# SCANNING ACTIVITY GRAVIMETRIC ANALYSIS (SAGA) OF AQUEOUS POLYETHYLENE OXIDE

Thesis by

Adam P. Olsen

In Partial Fulfillment of the Requirements for the

Degree of

Doctor of Philosophy

CALIFORNIA INSTITUTE OF TECHNOLOGY

Pasadena, California

2006

(Defended 23 May 2006)

# ACKNOWLEDGEMENTS

I would like to thank Rick Flagan and Julie Kornfield, my academic advisors, for their insightful guidance and unwavering support. It has been a pleasure to share this long and challenging journey with two mentors who maintained their enthusiasm for the project and faith in my abilities throughout. I would also like to thank Zheng-Gang Wang and John Seinfeld for evaluating this work as members of my thesis committee.

I have been fortunate to work alongside many talented and enjoyable students and postdocs at Caltech. I would like to thank them all, especially Dean, Junhong, Mohan, Tracey, Tim, Tomtor, Sally, Lucia, Nick, and Harmony for much needed comic relief and the occasional scientific discussion.

I have had the opportunity to discuss various topics with Chris Sorenson and Matthew Berg of Kansas State University, Nitash Balsara of University of California, Berkeley, Pavel Svitek of Measurement Science Enterprise, Inc., and Zhen-Gang Wang, George Gavalas, Bill Bridges, and Gary Lorden here at Caltech. Each has contributed to this thesis by providing a unique perspective from his area of expertise.

Marcy Fowler and Anne Hormann have been indispensible in arranging meetings and finding available research funds. Suresh Guptha has helped me immensely with timely computing support. Mike Vondrus has been a great resource as I learned how to do much of my own machining.

The majority of financial support for this work came from the National Science Foundation (NSF) Materials Research Science and Engineering Centers (MRSEC). During my first year on campus I was also supported by the William H. Corcoran Memorial Fellowship Fund.

Finally, I would like to thank my parents, Vikki and Paul, who have always encouraged my independence and curiosity. I would not have attempted, much less completed, this thesis if not for the love and trust they have given me throughout my life.

# ABSTRACT

This thesis introduces a new technique—scanning activity gravimetric analysis (SAGA)—for investigating phase transitions in semicrystalline polymers. Isothermal growth and dissolution of polymer crystallites within picogram to milligram samples are manifested by mass changes in response to changes in the activity of sorbed solvent vapor. Single charged particles are levitated and weighed in an electrostatic field, providing access to highly supersaturated states. Phase transitions are inferred from simultaneous equilibrium sorption and light scattering measurements. Analogous to differential scanning calorimetry, scanning solvent activity up and down exposes broad transitions between the semicrystalline solid state and the dissolved state, which are influenced by sample history. We demonstrate dissolution and crystallization of nanogram samples of polyethylene oxide by controlling the activity of sorbed water vapor and observe self-nucleation of crystallites from partially states and fully dissolved states.

Memory effects in semicrystalline polymers have been documented for a variety of systems in which the rate of crystallization depends on the temperature and duration of a prior melting step. We report analogous observations of memory effects in aqueous solution droplets of polyethylene oxide. Remnants of the crystalline phase—clusters of chain folded molecules—that are too small to be detected by gravimetric or optical means persist for long times in solution after macroscopic crystals have been dissolved, and they then serve as athermal nuclei when the concentration of the polymer solution droplet is increased. These remnants evolve under certain conditions toward increasing or decreasing thickness, as indicated by a shift in the conditions at which they effectively catalyze crystal growth. Although memory effects in semicrystalline polymers have usually been attributed exclusively to sluggish kinetics of melting or dissolution, thermodynamic considerations may also play an important role. A simple model describing the free energy of a lamellar crystal based on insights of Janeschitz-Kriegl captures the metastability of lamellar remnants and their evolution in thickness. The qualitative successes of the model lend support to the thermodynamic rationalization of memory effects in semicrystalline polymers.

# TABLE OF CONTENTS

# LIST OF TABLES AND FIGURES

## *Chapter 1*

# INTRODUCTION

## 1.1 SEMICRYSTALLINE POLYMER MORPHOLOGY

Crystallization of polymers is a first-order phase transition that is complicated by severe kinetic frustration, a metastable endpoint, and the potential for a single molecule to participate in multiple crystallites. A polymer melt or concentrated solution consists of countless entangled chains with random orientation and conformation. This morphology adds complexity to the physics of forming an ordered crystalline phase since chains must disengage from one another in addition to obtaining the correct conformation. Although the most stable crystal would involve the regular packing of completely outstretched chains, no real system can achieve such thermodynamic equilibrium, leaving all crystalline polymers in a metastable, semicrystalline state [1]. The morphology of the bulk crystalline phase typically demonstrates order on multiple length scales [2]. At the onset of crystallization, the random chains organize into chain-folded platelets or ribbons known as lamellae (Figure 1.1a). These lamellae grow radially outward and branch to form spherical superstructures known as spherulites (Figure 1.1b). Spherulites also include a significant fraction of noncrystalline material that fills the space between lamellae and sequesters severe entanglements or defects.

## 1.2 KINETICS OF CRYSTAL NUCLEATION AND GROWTH

The kinetics of crystal nucleation and growth from the melt vary strongly with temperature, exhibiting a maximum as temperature decreases from the equilibrium melting point to the glass

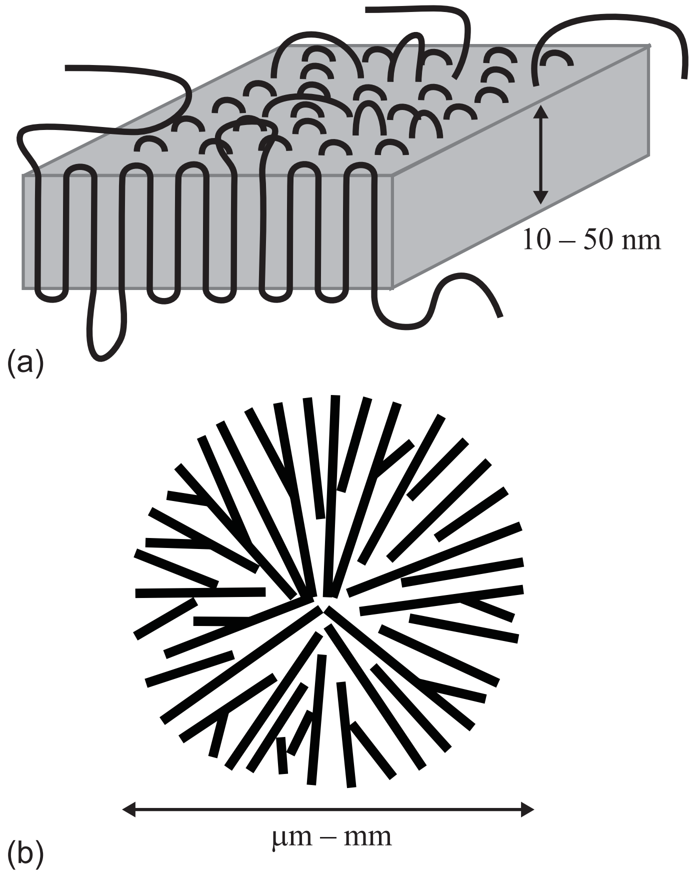

Figure 1.1. (a) Schematic of a lamellar polymer crystal depicting chain-folded molecules. (b) Schematic of a polymer spherulite in which many lamellae grow and branch radially outward from a nucleation site.

transition—a compromise between increasing energetic driving force and decreasing diffusive chain mobility. While theoretical models of crystal *growth* have been well developed for decades [3], the nature of the "nucleation event" in polymer crystallization is still debated. In the classical view, quiescent crystallization is initiated by homogeneous, or thermal, nucleation, which is driven by statistical thermal fluctuations in chain conformation in a supercooled melt or supersaturated solution. Fluctuations that result in a volume of the stable crystalline phase larger than some critical size will continue to grow; those that are smaller will rapidly die out. Recent experimental observations, however, have suggested that other processes may play a significant role under certain conditions. Several researchers, for example, claim to have observed a spinodal-like liquid-liquid separation prior to the emergence of crystals after a deep temperature quench [4, 5]. Another study revealed a strong correlation between crystallization kinetics and the time that a polymer sample was held above the observed melting point [6]; Janeschitz-Kriegl has suggested that crystallization in this instance was initiated by remnants of dissolved lamellae that serve as athermal nuclei [7] at sufficiently low temperature [8-10].

## 1.3 EXPERIMENTAL TECHNIQUES

A diversity of methods has been used to characterize the kinetics of polymer crystallization from the melt, including differential scanning calorimetry (DSC) [6, 11-15], temperature-modulated differential scanning calorimetry (TMDSC) [16-19], simultaneous small- and wide-angle X-ray scattering (SAXS/WAXS) [4, 5, 20, 21], optical microscopy [22, 23], and atomic force microscopy (AFM) [24]. This thesis introduces a new technique—scanning activity gravimetric analysis (SAGA)—that provides complementary observations to help further our understanding of this puzzling physical process. SAGA utilizes electrostatic levitation of single micron-sized particles [25] to investigate dissolution and growth of polymer crystals by manipulating the sorbed solvent content of a sample. This strategy enables direct manipulation of the chemical potential under isothermal conditions, so that the thermodynamic and kinetic parameters of a polymer crystal do not vary during an experiment, as they inherently do with thermal studies. Small sample volume and the absense of container surfaces provide access to highly supersaturated states in concentrated polymer solution that are essential for studies of nucleation kinetics. SAGA has been used to characterize many phenomena that are unique to polymers, including the morphological evolution of metastable crystallites and "memory" of the crystalline phase that often persists after all direct evidence of crystallinity has disappeared in a melt or solution.

## 1.4 THESIS OUTLINE

We begin by describing an automated single particle electrostatic levitation system that enables strict control of the temperature and chemical potential in nanogram samples of hygroscopic materials (Chapter 2). We then introduce SAGA as a technique for investigating polymer crystallization from highly concentrated polymer solutions and demonstrate phenomena analogous to that observed by DSC (Chapter 3). We continue by presenting results from a series of experiments in aqueous polyethylene oxide that support Janeschitz-Kriegl's theory of athermal polymer nucleation and also a model that rationalizes the evolution of small lamellar remnants in solution (Chapter 4). Finally, we propose continued studies that build on the present work (Chapter 5).

# REFERENCES

1 S. Z. D. Cheng, A. Keller, *Annu. Rev. Mater. Sci.* 28, 533 (1998).

2 G. R. Strobl, *The Physics of Polymers: Concepts for Understanding their Structures and Behavior* (Springer-Verlag, Berlin, 1996).

3 J. D. Hoffman, G. T. Davis, J. I. Lauitzen Jr., *The rate of crystallization of linear polymers with chain folding. In Treatise on solid state chemistry*, N.B. Hannay, Ed., (Plenum, New York, 1976) vol. 3, ch. 7, 497-614.

4 M. Imai, K. Mori, T. Mizukami, T. Kanaya, *Polymer* 33, 4451 (1992).

5 N. J. Terrill, P. A. Fairclough, E. Towns-Andrews, B. U. Komanschek, R. J. Young, A. J. Ryan, *Polymer* 39, 2381 (1998).

6 G. C. Alfonso, A. Ziabicki, *Col. Polym. Sci.* 273, 317 (1995).

7 J. C. Fischer, J. H. Hollman, D. Turnbull, *J. Appl. Phys.* 19, 775 (1948).

8 H. Janeschitz-Kriegl, *Col. Polym. Sci.* 275, 1121 (1997).

9 H. Janeschitz-Kriegl, E. Ratajski, H. Wippel, *Col. Polym. Sci.* 277, 217 (1999).

10 H. Janeschitz-Kriegl, *Col. Polym. Sci.* 281, 1157 (2003).

11 B. Fillon, J. C. Wittman, B. Lotz, A. J. Thierry, *Polymer Sci.* 31, 1383 (1993).

12 T. X. Liu, Z. S. Mo, S. G. Wang, H. F. Zhang, *Poly. Eng. Sci.* 37, 568 (1997).

13 Z.-G. Wang, B. S. Hsiao, B. B. Sauer, W. G. Kampert, *Polymer* 40, 4615 (1999).

14 A. Alizadeh, L. Richardson, L. Xu, S. McCartney, H. Marand, Y. W. Cheung, S. Chum, *Macromolecules* 32, 6221 (1999).

15 H. Marand, Z. Huang, *Macromolecules* 37, 6492 (2004).

16 I. Okazaki, B. Wunderlich, *Macromolecules* 30, 1758 (1997).

17 K. Ishikiriyama, B. Wunderlich, *Macromolecules* 30, 4126 (1997).

18 R. Androsch, *Polymer* 40, 2805 (1999).

19 A. Toda, C. Tomita, M. Hikosaka, Y. Saruyama, *Polymer*, 39, 5093 (1998).

20 A. M. Jonas, T. P. Russell, D. Y. Yoon, *Macromolecules* 28, 8491 (1995).

21 K. N. Krüger, H. G. Zachmann, *Macromolecules* 26, 5202 (1993).

22 M. V. Massa, J. L. Carvalho, K. Dalnoki-Veress, *Eur. Phys. J. E* 12, 111 (2003).

23 G. C. Alfonso, T. P. Russell, *Macromolecules* 19, 1143 (1986).

24 J. K. Hobbs, C. Vasilev, A. D. L. Humphris, *Polymer* 46, 10226 (2005).

25 E. J. Davis, *Aerosol Sci. Tech.* 26, 212 (1997).

*Chapter 2*

# A SINGLE PARTICLE LEVITATION SYSTEM FOR AUTOMATED STUDY OF HOMOGENEOUS SOLUTE NUCLEATION

## 2.1 INTRODUCTION

Levitated, micron-sized particles are advantageous for studies of nucleation. Elimination of container surfaces that might catalyze nucleation and isolation of microscopic sample volumes allow access to highly supersaturated states. The large surface to volume ratio of small levitated samples enables rapid equilibration of heat and mass transport, and thereby minimizes the measurement time. Electrostatic forces provide a convenient means to levitate and weigh individual charged particles in an applied electric field [1]. Electrostatic levitation has therefore found many applications in aerosol and materials research, including investigations of aqueous solution thermodynamics and crystal nucleation kinetics [1-12].

Several researchers have recently employed electrostatic levitation to quantitatively investigate crystal nucleation kinetics in a variety of chemical systems. Nucleation is a stochastic process; when a supersaturated or supercooled state is created, nucleation occurs after a delay or incubation time. From repeated measurements of this incubation time in levitated droplets under similar conditions, a number of authors have inferred nucleation rates. Krämer and co-workers [10] measured the nucleation rate of ice crystals in supercooled water by repeatedly injecting and trapping warm droplets in a cold balance; in a similar experiment Weidinger and co-workers [12] measured homogeneous and heterogeneous crystal nucleation rates from n-alkane melts. Both studies detected crystallization through changes in optical properties. In studies of nonvolatile solute in a volatile solvent, particle mass abruptly changes at the phase transition, providing a clear indicator of crystallization or dissolution. Supersaturated aqueous solution droplets maintain a metastable equilibrium at the water activity of the surrounding atmosphere until crystallization initiates spontaneous evaporation of water [2-5]; the mass loss is readily detected as a change in the levitation voltage. Hamza and co-workers [9] investigated nucleation kinetics of potassium chloride in supersaturated aqueous solution by repeatedly injecting dilute droplets into a balance with fixed relative humidity. Knezic and co-workers [8] measured the nucleation rate of a protein in aqueous droplets by cycling one particle between wet and dry states.

Crystal nucleation rates are extremely sensitive to thermal and chemical conditions [13]. When, for example, Krämer and co-workers [10] systematically varied the temperature, the measured ice crystal nucleation rate increased by a factor of 70 as the temperature was reduced by just 1 K. Precise control of the thermodynamic state is thus critical to the measurement of nucleation rates. Only able to regulate the relative humidity within ± 0.5% RH during repeated experiments, Hamza and co-workers [9] reported nucleation rates that varied by a factor of 300. Since single particle nucleation studies require many observations to characterize each particular state, experimental reproducibility and efficiency are paramount. For aqueous solution experiments in particular, one must incorporate robust control systems for maintaining the desired relative humidity and temperature to ensure reproducibility.

Precise control of relative humidity in the vicinity of a levitated particle is required for investigations of aqueous solution thermodynamics and solute nucleation kinetics as highlighted above. Cohen and co-workers [4] slowly flowed a prescribed mixture of dry and saturated air streams through a large enclosure containing the levitation electrodes to minimize aerodynamic particle disturbance. Liang and Chan [5] developed a quasiequilibrium technique that reduced the time required for experiments performed over a range in relative humidity. Using an instrument similar to that of Cohen and co-workers [4], they continuously monitored particle mass during the transient buildup of relative humidity after a step change in the inlet flow. Tang and Munkelwitz [3], Richardson and Spann [2], and Knezic and co-workers [8] employed a vacuum technique in which the working gas was pure water vapor and relative humidity was determined by the total pressure.

The aforementioned techniques all require that a particle be levitated and monitored for an extended time. Ideally, one would trap the particle in a stable potential well, however, according to Earnshaw's theorem, there are no local maxima or minima in a three-dimensional electrostatic field, only saddle points. A stable electrostatic levitation system cannot therefore be constructed; purely electrostatic levitation requires active control. Each of the studies highlighted above, in fact, utilized a stable variation of electrostatic levitation known as electrodynamic levitation [14, 15]. A conventional electrodynamic levitator balances charged particles against gravity with a vertical DC electric field and stabilizes them with an axisymmetric AC field [1]. Many geometrical variations can successfully levitate particles [16]; a particularly simple configuration is an AC ring electrode in the horizontal plane midway between two plates of a capacitor. A DC potential across the capacitor creates a vertical electric field for balancing gravitational forces. A potential applied to the ring creates a saddle point in the equipotential map of any vertical plane. When an AC potential of appropriate amplitude and frequency is applied to the ring, particles experience a time-averaged force towards the geometric null point. This dynamic stability allows the particle to be confined indefinitely to a finite volume of space. Unbalanced particles oscillate at the frequency of the AC potential. Vertical oscillations are eliminated only when the vertical DC electric field is adjusted to exactly balance gravity. Stray lateral fields can cause horizontal oscillations as well; several researchers have eliminated these by adding compensating lateral DC fields [17, 18]. Zheng and co-workers [19] introduced an elegant design in which vertical and horizontal DC biases could be applied to a segmented AC ring electrode for three-dimensional compensation.

The electrodynamic levitator naturally lends itself to being controlled. The particle's position can be determined optically, and automated feedback control can be implemented to maintain the proper balancing potential [20, 21]. The DC potentials required to balance a particle are proportional to external forces, so the vertical DC balancing potential provides a record of particle mass. The controller must be precisely aligned with the null point of the AC field to minimize particle oscillations, however, and any mechanical or electronic drift will reduce the accuracy of the mass measurement. Electrodynamic levitators with lateral compensation or purely electrostatic levitators may be integrated with three-dimensional position controllers to enable long term particle confinement [18, 22]; these systems enable a more robust mass measurement since they do not require precise alignment with the dynamic null point.

This chapter describes a system for gravimetric analysis of nucleation from solution. The instrument employs an electrostatic particle levitator with a three-dimensional position controller; the levitator can also be operated as an electrodynamic balance by coupling the horizontal compensation electrodes to an AC potential. The instrument also incorporates strict temperature regulation and automated relative humidity control that is based on a novel continuous flow technique. The humidity controller is programmable, enabling exposure to any desired history, and experiments are fully automated for superior efficiency and reproducibility. Accuracy of relative humidity control and mass measurement was verified by comparing the measured thermodynamics of aqueous sodium chloride solution droplets with a reported correlation. The instrument is programmed to accumulate statistics of nucleation incubation times; nucleation statistics and inferred rates for a supersaturated sodium chloride droplet are reported.

## 2.2 APPARATUS

The particle levitation instrument is assembled from machined components, custom electronics, and commercially available devices. All electronic components are integrated with a PC equipped with data and image acquisition boards, enabling experiments that are automated and thus highly reproducible. The user interface is programmed in LabView.

### 2.2.1 Levitation Electrodes and Environmental Chamber

The electrode configuration depicted in Figure 2.1 consists of two DC disk electrodes ($E_{z+}$ and $E_{z-}$) located above and below the particle and a coaxial cage of eight rod electrodes arranged on a regular octagon. Horizontal electrostatic forces can be generated by application of a symmetric DC bias between opposing pairs of rods (Table 2.1). The geometry closely resembles that employed by Schlemmer and co-workers [23], although the symmetry axis in that work was horizontal. The electrodes allow three-dimensional electrostatic force compensation so that a particle can be trapped indefinitely with proper feedback control, while allowing optical access along four coplanar axes.

Table 2.1. Time dependent electric potentials applied to each of the six levitation electrodes and operating voltage limits

| Electrode | Potential |
|---|---|
| $E_{x+}$ | $V_x + V_{AC} \cos \omega t$ |
| $E_{x-}$ | $-V_x + V_{AC} \cos \omega t$ |
| $E_{y+}$ | $V_y + V_{AC} \cos \omega t$ |
| $E_{y-}$ | $-V_y + V_{AC} \cos \omega t$ |
| $E_{z+}$ | $V_z$ |
| $E_{z-}$ | $-V_z$ |
| $V_{AC} < 2000$ V @ 30 – 300Hz | |
| $\|V_x\| < 15$ V | |
| $\|V_y\| < 15$ V | |
| $\|V_z\| < 150$ V | |

This levitator can also be operated as an electrodynamic balance by biasing all of the cage electrodes with an AC potential. In practice, electrodynamic mode is used to capture a particle; $V_{AC}$ is then decreased to zero during all experiments. The AC electric field generated by this electrode configuration (Figure 2.2a,c) is highly axisymmetric in the vicinity of the particle even though the AC electrode is a discrete cage. The AC saddle point evident in Figure 2.2a is responsible for electrodynamic focusing. The axial (Figure 2.2b) and lateral (Figure 2.2d) components of the DC electric field enable electrostatic balancing against gravitational, aerodynamic, and Brownian forces.

The electrodes are housed inside a machined stainless steel chamber that enables strict control of the particle's environment. The chamber body has an octagonal perimeter and a cylindrical internal cavity with an internal volume of approximately 40 cc (Figure 2.3). Eight view ports

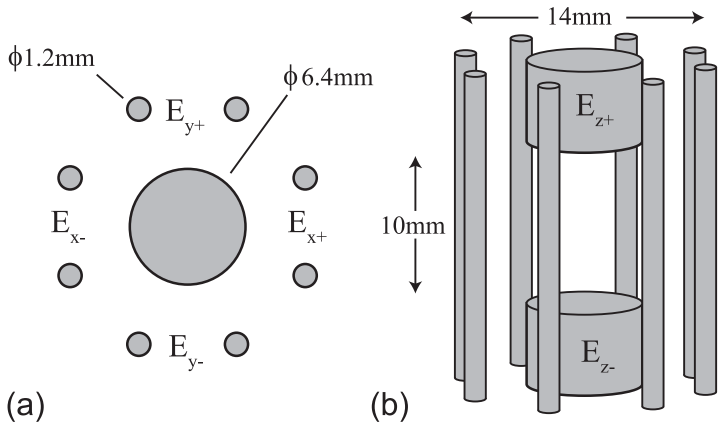

Figure 2.1. Schematic of the electrode configuration designed for electrostatic and electrodynamic particle levitation showing (a) the top view and (b) a three-dimensional representation. Each of the six isolated electrodes are labeled.

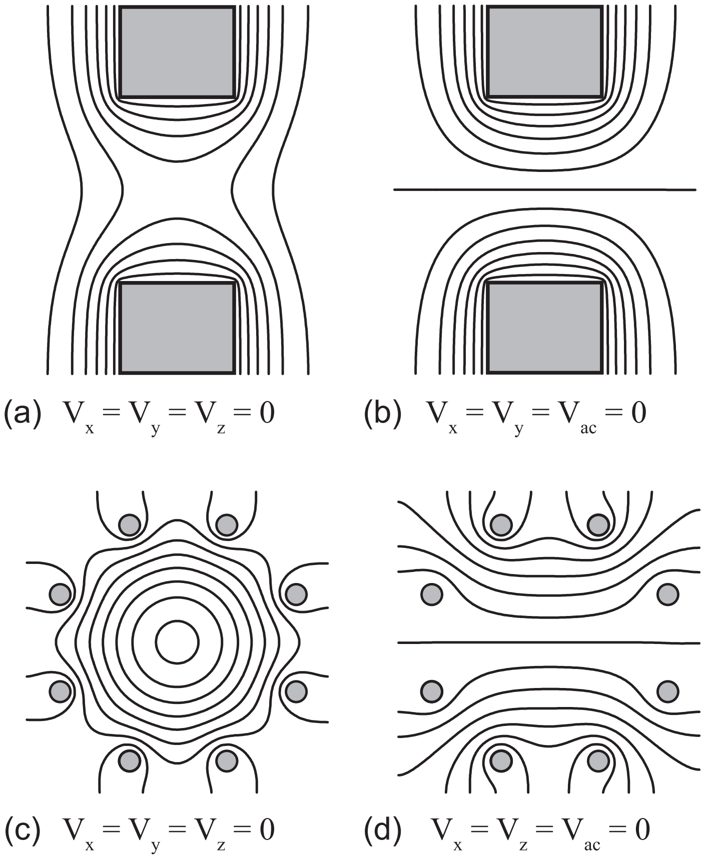

(a) $V_x = V_y = V_z = 0$ (b) $V_x = V_y = V_{ac} = 0$

(c) $V_x = V_y = V_z = 0$ (d) $V_x = V_z = V_{ac} = 0$

Figure 2.2. Calculated equipotential contours in the x = 0 plane for (a) the AC field and (b) the z DC field, and in the z = 0 plane for (c) the AC field and (d) the y DC field using the ion optics simulation software SIMION. Since Laplace's equation is linear, the total electric field is the sum of all component fields.

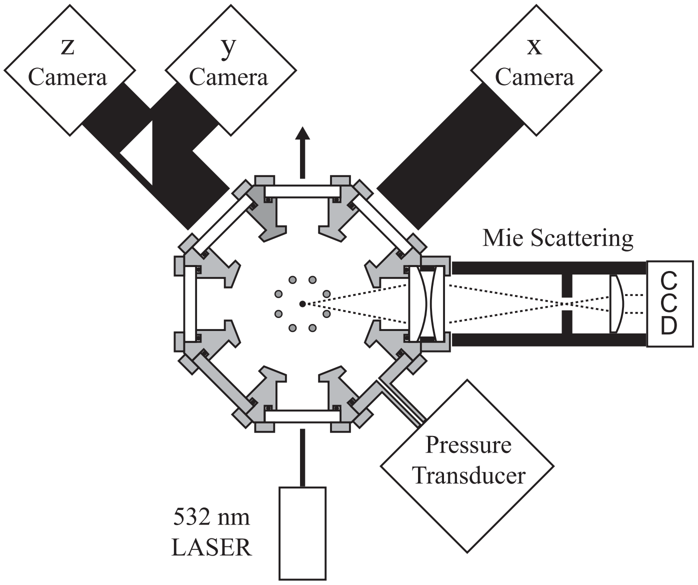

Figure 2.3. Sectional view of the levitation chamber in the z = 0 plane and peripheral components. Three linescan cameras detect particle displacement in x, y, and z directions as indicated.

permit optical access to the particle between adjacent rod electrodes. The view ports provide 0.17 sr (24 degrees) of access for laser illumination, particle imaging, and collection of angular light scattering. The body has annular channels machined into the sidewall above and below the plane of the view ports through which a heat transfer fluid can be circulated to attain precise temperature control (Figure 2.4). Stainless steel end caps seal the chamber body from above and below. The chamber temperature is continuously monitored by two thermistors, one mounted to each end cap. An annular stainless steel frit (Mott Corporation) secured above an annular channel in the internal face of each end cap defines a balanced upwards gas flow through the chamber. The resulting flow pattern enables rapid turnover of internal gas composition while minimizing the aerodynamic drag force on the particle. The electrode assembly is secured to and electrically isolated from the end caps via ceramic feedthroughs. All joining surfaces are sealed with viton o-rings.

A hole though the center of the bottom DC electrode facilitates capture of solid particles from a powdered sample according to the following procedure. An ensemble of particles is introduced to the interior of the chamber on the tip of a dielectric rod, and with the AC field adjusted safely below breakdown level, a mechanical pulse launches one or more particles into stable oscillation. A target particle is then isolated by appropriate adjustment of the DC potentials and reduction of the AC potential. The access hole is plugged and sealed during the experiment by a delrin rod capped with stainless steel (Figure 2.4).

### 2.2.2 Particle Imaging and Position Control

Three-dimensional imaging and position control confines a particle within a finite viewing volume and provides a continuous record of particle mass. The levitated particle is illuminated

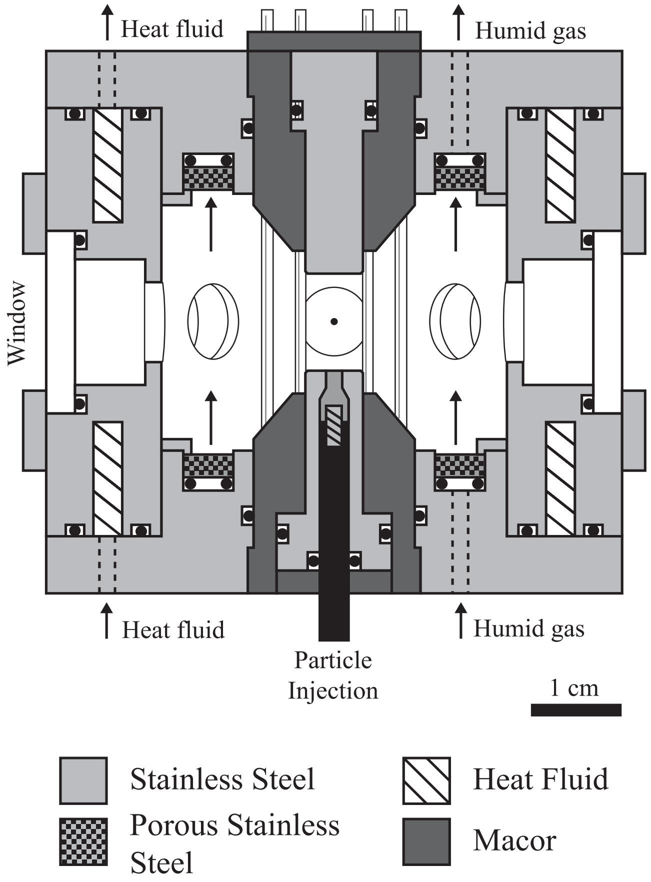

Figure 2.4. Sectional view of the levitation chamber in the plane of the laser beam. Rod electrodes are positioned out of this plane and the plane of all optical axes as shown in Figure 2.3.

by a linearly polarized 25 mW 532nm diode laser beam (Melles Griot) (Figure 2.3). Microscope tubes image the particle onto each of three mutually orthogonal analog CCD linescan cameras (Perkin Elmer; LC3000). A beam splitter in one of the optical paths enables two orthogonal axes (y and z) to be imaged through a single view port. A cylindrical lens in each optical path generates a line image perpendicular to the detector array. These x, y, and z images are digitized by a multichannel framegrabber (Bitflow, Inc.; Raven). A digital PID (Proportional + Integral + Derivative) algorithm generates x, y, and z DC control voltages to maintain the particle at the intersection of both imaging axes and the laser beam. The controller operates at 40 Hz and is sufficient to stably confine particles in electrostatic mode without dynamic focusing.

The PID parameters are empirically determined for optimum performance. With proper tuning, the position controller is sufficiently sensitive to hold a levitated particle during the most rapid transients in mass that are anticipated for a given experiment without introducing excessive fluctuations at steady state. If the mass changes so rapidly that the controller cannot maintain the particle within the viewing volume, the control software is programmed to briefly activate the AC field until the particle image is reacquired. This failsafe is occasionally needed after a nucleation event.

### 2.2.3 Relative Humidity Control

A novel technique for controlling the relative humidity inside the levitation chamber enables rapid and stable control of the concentration of levitated aqueous solution droplets. A constant mass flow rate (ca. 75 sccm) of gas through the chamber is maintained by simply placing a limiting orifice (O'Keefe Controls; 10 micron) ahead of a diaphragm vacuum pump as shown in the upper right of Figure 2.5. An environmental control module regulates the total pressure inside the levitation chamber as it is continuously purged by a nitrogen stream that has been humidified to a fixed high relative humidity. The relative humidity inside the chamber is controlled by adjusting the pressure. A Nafion membrane shell-and-tube humidifier (Perma Pure Inc.) generates a near saturated flow of humid nitrogen (ca. $10^3$ sccm) and a high performance humidity sensor (Vaisala; HMP230) continuously monitors the humidity at ambient pressure ($p_o$). The humidifier and relative humidity probe are maintained at the same temperature as the levitation chamber with circulating heat transfer fluid for stability. The recirculation bath (Neslab; RTE 7) has both heating and cooling capacity and is filled with a mixture of water and ethylene glycol for temperature control between –25 and 125 ± 0.01 °C. A proportional solenoid valve (Pneutronics; Lone Wolf) located just upstream from the levitation chamber serves as a variable pressure drop flow element for adjusting the total pressure inside the chamber. A transducer (MKS Instruments, Inc.; 222B) installed in one of the chamber access ports continuously monitors the chamber pressure (p), which is digitized along with the output of the relative humidity sensor ($RH_o$). The relative humidity at the particle ($RH_p$) is then: $RH_p = (p/p_o)\ RH_o$. A digital PID control algorithm generates a control voltage for the proportional solenoid valve to keep $RH_p$ at the specified value inside the levitation chamber. The controller operates at 40 Hz and can be programmed to expose a levitated particle to any desired relative humidity history. In practice this technique enables stable control of relative humidity up to 95% RH.

### 2.2.4 Collection of Angular Light Scattering

Angularly resolved scattered light from a levitated particle is collected through one of the view

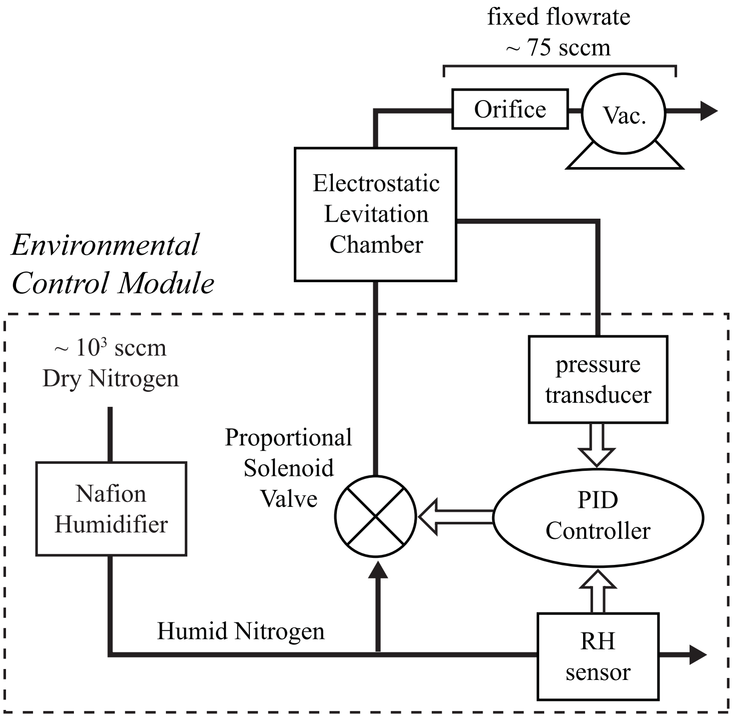

Figure 2.5. Schematic of the environmental control module.

ports orthogonal to the illuminating laser beam (Figure 2.4). The optical arrangement is similar to that reported by Krämer and co-workers [10]. A collimating lens fastened directly to the chamber in place of a window minimizes Fabry-Perot interference that would result from passing the spherical wavefront through the two parallel flat surfaces of a window. A second lens focuses the scattered light through an aperture (approximately 1.5 mm) to filter off-axis radiation and a third lens recollimates the light onto the CCD detector of a video camera. The resulting unfocused particle image maps scattered light intensity as a function of scattering angle between approximately 78° and 102° relative to the illuminating laser beam. The images can be used to determine the size of liquid droplets by comparison with Mie theory [24]. Upon formation of heterogeneities in the supersaturated liquid, deviation from Mie scattering is observed. Conversely, when heterogeneities dissolve away, the Mie pattern reemerges. Thus, the images provide direct evidence of crystal nucleation and dissolution.

## 2.3 RESULTS

### 2.3.1 Instrument Characterization

Angularly resolved light scattering provides an estimate of absolute sample size and can be used to differentiate liquid droplets and solid particles. The scattering image of the aqueous sodium chloride droplet reveals vertical fringes characteristic of an isotropic sphere (Figure 2.6a); the fringe spacing indicates a diameter of 30 ± 1 microns from comparison with Mie theory. The scattering image of a sodium chloride particle in the dry crystalline state is uncorrelated, indicating optical heterogeneity (Figure 2.6b).

The long term stability of the instrument's humidity control was demonstrated by holding an aqueous sodium chloride droplet at 75% RH and 21 °C for 8 hours (Figure 2.7). The recorded

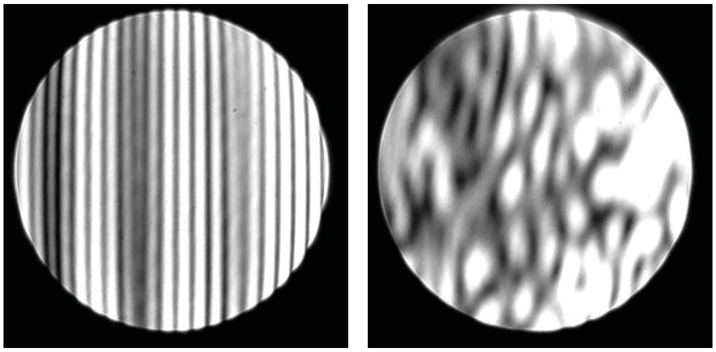

(a) $m/m_o = 3.0$ (b) $m/m_o = 1.0$

$D_p = 30$ microns

Figure 2.6. Light scattering images of (a) and aqueous sodium chloride droplet and (b) a dry sodium chloride particle. Each image resolves light scattered between 78° and 102° relative to the incident laser beam.

mass has been normalized by the 8 hour average and indicates deviation of less than ± 0.1%. If we assume that the droplet rapidly equilibrates with the water vapor in the surrounding atmosphere, the relative humidity at the droplet can be calculated from the known water activity of sodium chloride solutions [25], as is illustrated by the black trace in Figure 2.7a. This analysis allows estimation of the RH standard deviation: $\sigma = 0.03\%$ RH.

### 2.3.2 Aqueous Solution Thermodynamics

Hydrophilic crystalline materials such as sodium chloride exhibit an asymmetric response to humidification (Figure 2.8). The relative humidity controller was programmed to expose a levitated sodium chloride particle to a triangular ramp between 40% and 78% RH at a scan rate of 20% RH/hr. The temperature remained between 24.9 °C and 25.0 °C throughout the experiment. The vertical balancing voltage was continuously monitored by the position controller during electrostatic levitation. Relative mass was calculated by normalizing the instantaneous balancing voltage by the balancing voltage in the dry state. As the humidity increased, no water was absorbed until 75% RH, at which point the crystalline particle was spontaneously dissolved by uptake of water from the vapor to form a saturated aqueous solution droplet that continued to grow with further humidification. This transition is known as deliquescence. Reducing the humidity dried the droplet, increasing the solute concentration well above the saturation limit until, at approximately 50% RH, crystal nucleation initiated the sudden evaporation of all water and the particle returned to the dry state. This transition is known as efflorescence.

Pseudoequilibrium conditions apply during a sufficiently slow continuous scan. This can be verified by comparing the droplet mass as a function of RH with observations made when the

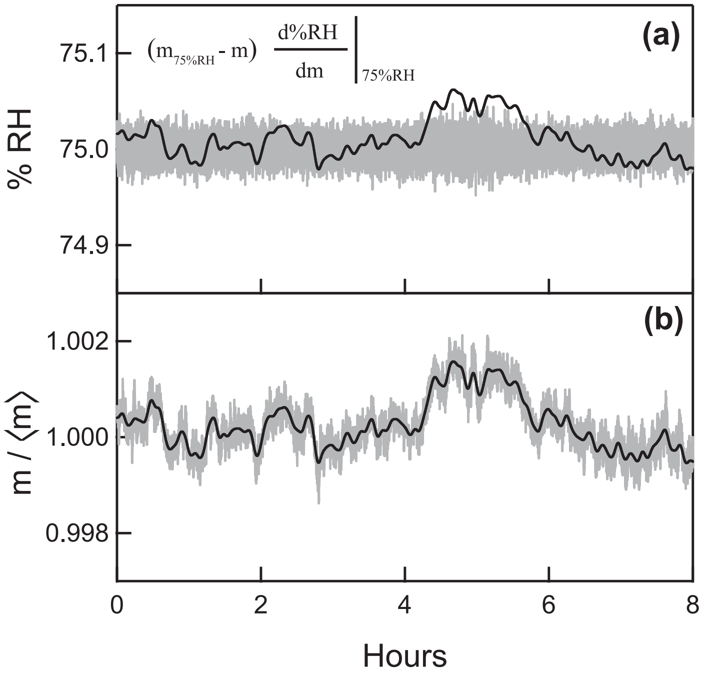

Figure 2.7. Stability of an aqueous sodium chloride droplet at constant relative humidity. Particle mass is normalized by the 8 hour average. Gray traces: raw data collected at 30 second intervals. Black traces: (a) calculated RH and (b) filtered droplet mass. T = 21 °C.

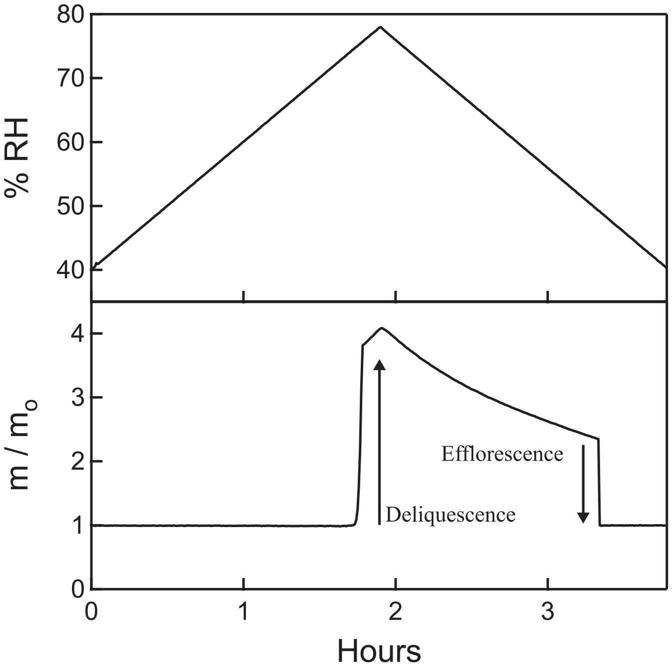

Figure 2.8. Response of a sodium chloride particle to a continuous triangular relative humidity scan at 20% RH/hr. Particle mass was normalized by the mass of the dry state. Data points are recorded at 30 second intervals. T = 25 °C.

RH is held constant sufficiently long to ensure that equilibrium is achieved. Measurements were made in discrete 30 minute steps from 55% to 80% RH (Figure 2.9). The solution concentration equilibrates rapidly compared to the step time; increasing and decreasing steps yield identical results.

The droplet mass measured with a 20% RH/hr scan agrees well with both the stepping-mode data and a correlation previously developed by Tang and co-workers [25] based on stepping-mode electrodynamic balance experiments (Figure 2.10). Repeated scans demonstrate the reproducibility of the thermodynamic (water activity) measurements. Small variations appear in the deliquescence RH ($RH_d$); larger variations appear in the efflorescence RH ($RH_e$). The latter deviations reflect the stochastic nature of crystal nucleation that we will explore below.

### 2.3.3 Nucleation Statistics

Solute nucleation is a stochastic process driven by fluctuations in a metastable solution. Once a stable nucleus forms, it rapidly grows, thereby producing an efflorescence event. The nucleation rate (number of events per unit volume per unit time) can be estimated as: $J = (\langle\tau\rangle V_p)^{-1}$, where $\langle\tau\rangle$ is the average incubation time and $V_d$ is the droplet volume. Reliable estimation of the nucleation rate therefore requires many efflorescence event observations. The instrument described above enables accumulation of incubation time statistics through (i) automated detection of droplet efflorescence at a well-defined RH and (ii) subsequent processing to rapidly and accurately restore the supersaturated state (Figure 2.11). A single sodium chloride particle was cycled unattended between a fully saturated state at 78% RH and a supersaturated state at 51% RH for 130 hours, during which time 78 nucleation events were observed. The temperature was maintained at 20.10 ± 0.05 °C throughout the experiment. A

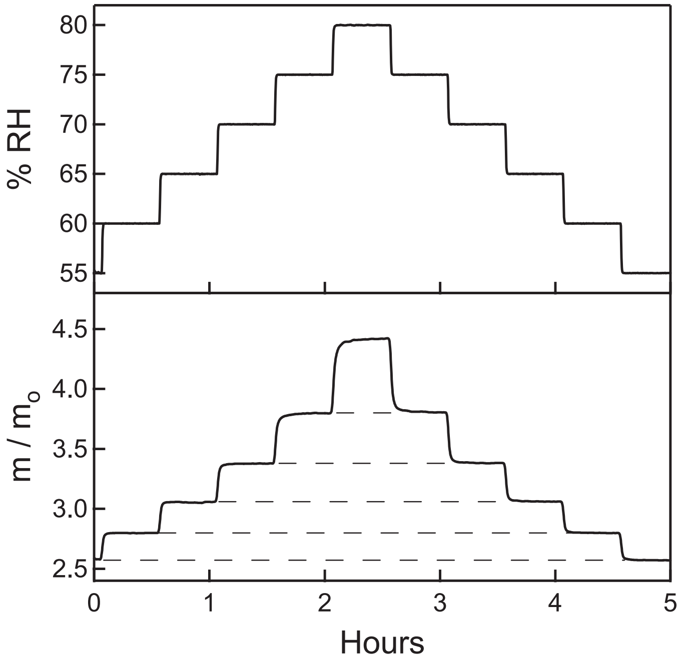

Figure 2.9. Response of a supersaturated aqueous sodium chloride droplet to relative humidity steps. Particle mass was normalized by the mass of the dry state. T = 25 °C.

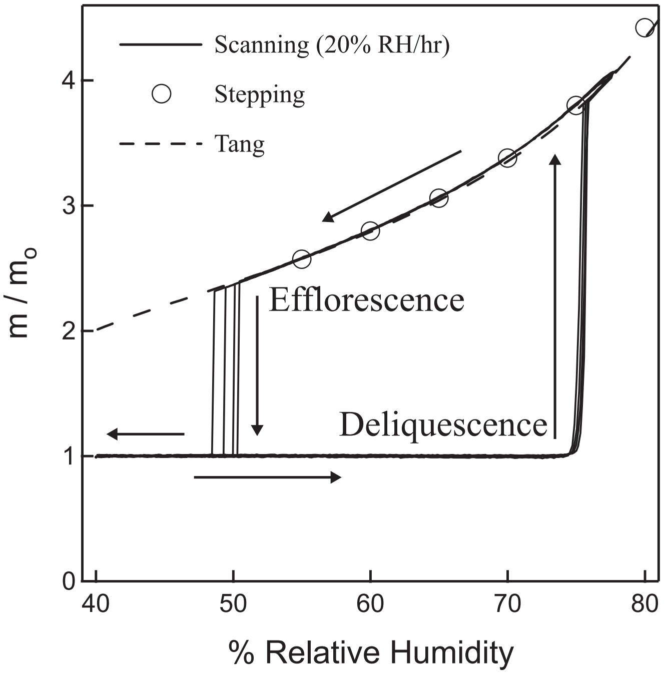

Figure 2.10. Parametric plot of thermodynamic data for a sodium chloride particle. Current experiments were compared to a correlation previously published by Tang. T = 25 °C.

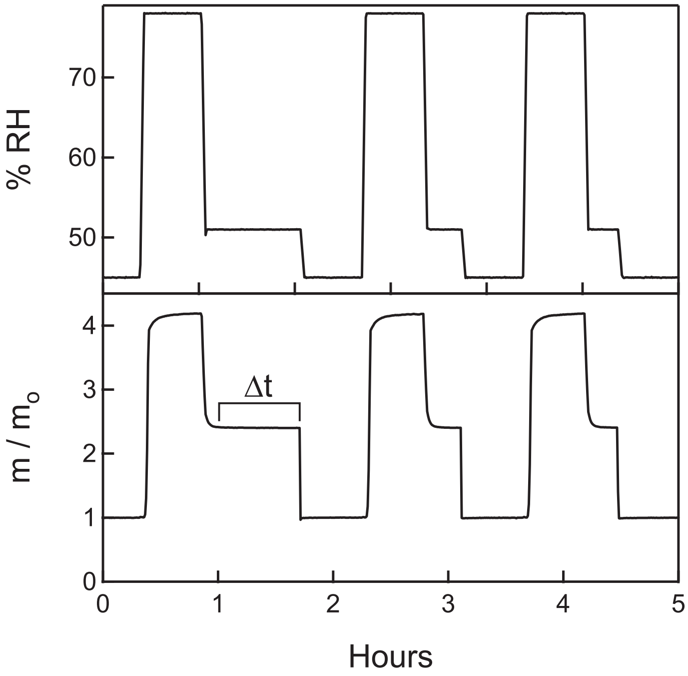

Figure 2.11. Programmed relative humidity history and particle response typical of the automated nucleation experiment.

dry crystalline sodium chloride particle deliquesces when the relative humidity is raised above 75%. When the relative humidity is then reduced to 51% the solution droplet equilibrates to a supersaturated state with a relative mass of 2.4. The droplet remains in this metastable state until a nucleation event initiates crystallization of the entire particle accompanied by complete evaporation of water. Immediately after each nucleation event was detected the RH was further decreased to, and held briefly at, 45% RH to thoroughly dry the particle and ensure a consistent starting point for the next cycle. While not essential for the present experiment, this additional drying is needed for materials that may retain water in the crystalline state, e.g., hydrophilic semicrystalline polymers that we are also probing with this apparatus. The abrupt reduction in mass to the dry state is automatically detected by software so that the cycle can be repeated. For each iteration the time between equilibration of the supersaturated state and nucleation is recorded as an incubation time.

Seventy-eight incubation times were compiled (Figure 2.12) to determine an average measured incubation time of 34 minutes, indicating that nuclei were formed at a rate of $4.9 \times 10^{-4}$ nuclei/droplet/s. If the probability of observing a nucleation event is time independent, nucleation can be modeled as a Poisson process; crystallization of an ensemble of identical supersaturated droplets will then obey first-order kinetics [26]. The ratio of uncrystallized droplets (N) to the total number of droplets ($N_o$) decays with time since the onset of supersaturation as predicted for a Poisson process, i.e., $\ln(N/N_o) = -t/\tau$ (Figure 2.13). The close approximation to exponential decay gives no basis for rejecting the Poisson model.

The droplet diameter at 51% RH is 33 microns as determined from Mie scattering images. The corresponding droplet volume ($1.9 \times 10^{-8}$ cm$^3$) enables calculation of a volumetric nucleation rate of 2.6 x $10^4$ nuclei/$cm^3$/s. Given this measured rate and the experimental sample size of 78, the actual nucleation rate is most likely bounded by 2.0 x $10^4$ and 3.2 x $10^4$ nuclei/$cm^3$/s, corresponding to a maximum uncertainty of ± 22% within the 95% confidence interval.

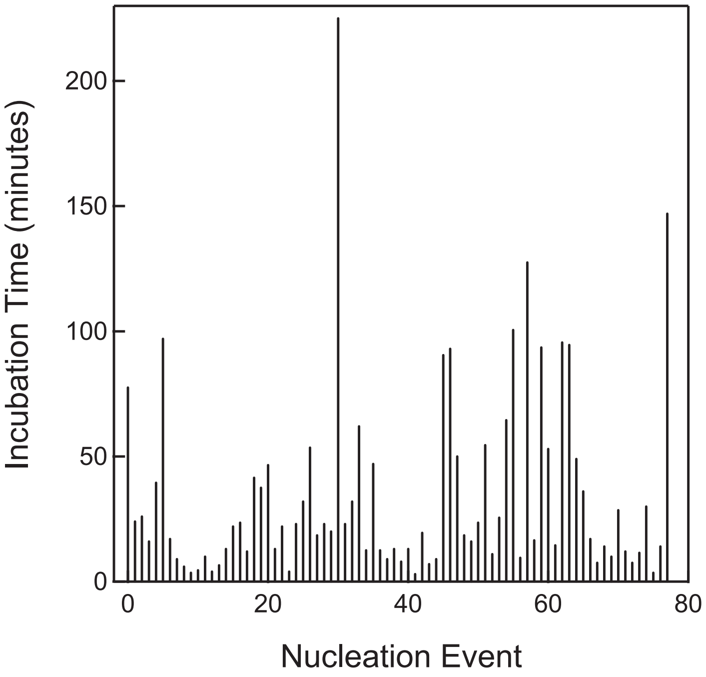

Figure 2.12. Nucleation incubation times recorded during the nucleation experiment. The average recorded incubation time was 34 minutes.

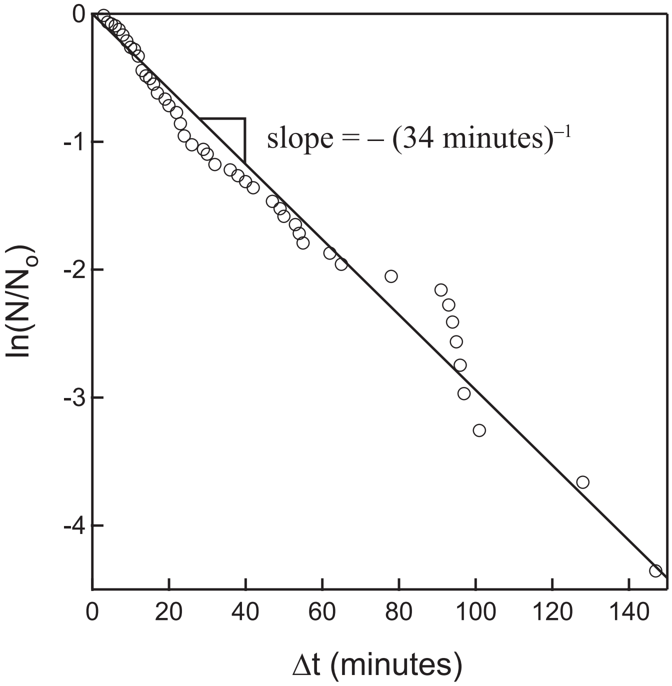

Figure 2.13. Natural logarithm of the fraction of uncrystallized droplets remaining vs. incubation time. The solid line represents exponential decay predicted by the average measured incubation time of 34 minutes.

# REFERENCES

1 E. J. Davis, *Aer. Sci. Tech.* 26, 212 (1997).

2 C. B. Richardson, J. F. Spann, *J. Aer. Sci.* 15, 563 (1984).

3 I. N. Tang, H. R. Munkelwitz, J. *Col. Int. Sci.* 98, 430 (1984).

4 M. D. Cohen, R. C. Flagan, J. H. Seinfeld, *J. Phys. Chem.* 91, 4563 (1987).

5 Z. Liang, C. K. Chan, *Aer. Sci. Tech.* 26, 255 (1997).

6 S. Oatis, D. Imre, R. McGraw, J. Xu, *Geo. Res. Let.* 25, 4469 (1998).

7 J. M. Lightstone, T. B. Onasch, D. Imre, *J. Phys. Chem. A* 104, 9337 (2000).

8 D. Knezic, J. Zaccaro, A. S. Myerson, *J. Phys. Chem. B* 108, 10672 (2004).

9 M. A. Hamza, B. Berge, W. Mikosch, E. Rühl, *Phys. Chem. Chem. Phys.* 6, 3484 (2004).

10 B. Krämer, O. Hübner, H. Vortisch, L. Wöste, T. Leisner, M. Schwell, E. Rühl, H. Baumgärtel, *J. Chem. Phys.* 111, 6521 (1999).

11 R. A. Shaw, D. Lamb, *Geo. Res. Let.* 26, 1181 (1999).

12 I. Weidinger, J. Klein, P. Stöckel, H. Baumgärtel, T. Leisner, *J. Phys. Chem. B* 107, 3636 (2003).

13 H. R. Pruppacher, *J. Atmos. Sci.* 52, 1924 (1995).

14 H. Straubel, *Z. Elektrochem* 60, 1033 (1956).

15 R. F. Wuerker, H. Shelton, R. V. Langmuir, *J. App. Phys.* 30, 342 (1959).

16 W. H. Hartung, C. T. Avedisian, *Proc. R. Soc. London A* 437, 237 (1992).

17 S. Arnold, *Rev. Sci. Instrum.* 62, 3025 (1991).

18 X. Zhang, E. Bar-Ziv, *Rev. Sci. Instum.* 67, 3483 (1996).

19 F. Zheng, X. Qu, E. J. Davis, *Rev. Sci. Instrum.* 72, 3380 (2001).

20 P. J. Wyatt, P. T. Phillips, *J. Col. Int. Sci.* 39, 125 (1972).

21 S. Arnold, *J. Aer. Sci.* 10, 49 (1979).

22 W. K. Rhim, S. K. Chung, D. Barber, K. F. Man, G. Gutt, A. Rulison, R. E. Spjut, *Rev. Sci. Instrum.* 64, 2961 (1993).

23 S. Schlemmer, J. Illemann, S. Wellert, D. Gerlich, *J. App. Phys.* 90, 5410 (2001).

24 H. C. van de Hulst, *Light Scattering by Small Particles* (Wiley, New York, 1957).

25 I. N. Tang, A. C. Tridico, K. H. Fung, *J. Geophys. Res.* 102, 23269 (1997).

26 D. Turnbull, *J. Chem. Phys.* 20, 411 (1952).

*Chapter 3*

# SCANNING ACTIVITY GRAVIMETRIC ANALYSIS (SAGA) OF AQUEOUS POLYETHYLENE OXIDE

## 3.1 INTRODUCTION

Many polymers crystallize to form chain-folded platelets or ribbons called lamellae that have thickness on the order of 10 nanometers and may grow beyond a micrometer in length and width [1]. Molecular segments repeatedly traverse the smallest dimension to create two high energy surfaces of folds and dangling chains that significantly destabilize lamellae relative to the equilibrium extended chain crystal, which is unattainable because of kinetic frustration associated with long entangled molecules. Polymer crystals are thus metastable structures [2]; lamellar thickness is determined not by thermodynamics, but by growth kinetics in a supercooled melt or supersaturated solution. Lamellae are separated by amorphous domains, which sequester severe entanglements or defects that are excluded by crystals; polymers, therefore, are typically classified as semicrystalline.

Nucleation processes figure prominently in both early and late stages of polymer crystallization [1, 3, 4]. Primary nucleation is the formation of a stable volume of ordered material from an amorphous melt or solution; it often occurs heterogeneously in the presence of foreign catalytic surfaces, but may also occur homogenously in samples that are free of impurities. Secondary nucleation, also called molecular nucleation [5], is the irreversible attachment of one or more stems of an amorphous polymer chain to a growing crystallite. Once anchored, the entire molecule is reversibly incorporated into the crystal. Both nucleation processes proceed at appreciable rates only far from equilibrium, which explains the unique metastability of partially melted polymer samples [6]. Few fundamental measurements of the rates of these important processes have been reported due to the difficulty of making direct observations that are not influenced by foreign surfaces or inclusions.

This chapter introduces the application of single particle levitation [7] to the study of semicrystalline polymers. Isolated micron-sized samples of polymer are levitated in an electrostatic field and exposed to solvent vapor at variable partial pressure. As the polymer sorbs and evaporates solvent, and consequently undergoes dissolution and crystallization transitions, sample mass and optical properties are continuously monitored. The large surface-to-volume ratio enables rapid equilibration of heat and mass transport within the sample, thereby minimizing the measurement time. The small volume also minimizes the likelihood that the sample contains foreign inclusions that may serve as heterogeneous nuclei. Levitated samples have surfaces that contact only a gas, in contrast with previous studies of polymer nucleation in which ensembles of dispersed droplets were in contact with foreign condensed matter [8-12].

A diversity of methods has been used to characterize the kinetics of crystallization in polymers [13-29]. Among these, the most widely implemented is differential scanning calorimetry (DSC), which provides a point of departure for the experimental methods presented below. Kinetics of crystallization are most frequently described in qualitative terms using the rate of heat evolution during cooling at a constant rate. For example, the effect of nucleating agents is often reported in terms of the upward shift of the temperature at which the maximum heat evolution rate occurs during cooling [22-24]. Here we show that analogous information can be obtained under isothermal conditions by decreasing the activity of a solvent.

Calorimetry has also been a powerful tool to probe the melting of lamellae, which typically occurs over a range of temperatures during heating at a constant rate. Coordinated DSC and SAXS (small-angle X-ray scattering) or AFM (atomic force microscopy) measurements have shown that the broad melting transition is largely due to the distribution of lamellar thickness present in the semicrystalline nanostructure; the thinnest lamellae melt at the lowest temperatures in the endotherm and progressively thicker lamellae contribute to the endotherm as temperature increases [17, 25]. Interestingly, heating to temperatures that completely melt all lamellae that can be detected by SAXS or microscopy, does not necessarily erase all memory of the previous solid state [26-31]; the microscopic basis of the "melt memory effect" is not yet well understood. Here we show that ramping up the activity of solvent exposes an analogous, broad dissolution isotherm, and that, upon reversal of the activity scan after dissolution of the lamellae, memory of the previous solid state affects the degree of supersaturation that must be reached to trigger regrowth of lamellae.

Scanning activity gravimetric analysis (SAGA) permits protocols analogous to DSC, such as constant scan rate up or down in activity or discrete jumps up or down in activity. Analogous to DSC measuring heat flux to a sample in response to changing temperature, SAGA monitors the absorption or evaporation of solvent in response to changing activity. The present work investigates crystal nucleation, growth, and dissolution in aqueous polyethylene oxide (PEO) under isothermal conditions.

## 3.2 EXPERIMENTAL

An automated single particle electrostatic levitation system, described in detail previously [32], was used to perform SAGA on PEO (Sigma Aldrich Co.; $M_w$ = 100,000 g/mol), scanning the activity of water. A three-dimensional electrostatic field generated by a cage of electrodes (Figure 3.1a) suspends a micron-sized charged particle against gravitational, aerodynamic, and Brownian forces; the DC balancing voltage ($V_b$) applied across the disk electrodes shown in Figure 3.1a is proportional to mass. Automated position control maintains the particle within a finite view volume defined by an illuminating laser beam as the sorbed water content equilibrates with the humid atmosphere. The balancing voltage is continuously recorded during an experiment, and relative mass ($m/m_o$) is calculated by normalizing the instantaneous balancing voltage by the balancing voltage in the dry state, i.e., $m/m_o = V_b/V_{b,dry}$.

The relative humidity (water activity, $a_w$) and temperature of a nitrogen atmosphere surrounding the particle are strictly regulated by an environmental control module (Figure 3.1b). The apparatus can be programmed to impose any desired water activity history; the experiments described below use simple constant rate scans. The humidity in the sample chamber equals that of the inlet stream at low to moderate water activity ($a_w < 0.80$). At high water activity ($a_w > 0.80$), the humidity at the sample slightly lags that of the inlet stream. A calibration procedure is implemented to correct for the instrument lag, as described in Appendix B.

Dissolution and crystallization are directly observed through changes in water content and optical properties. When all crystallites dissolve, the sample becomes a spherical droplet of polymer solution. A micron-sized optically homogeneous sphere, such as a small solution

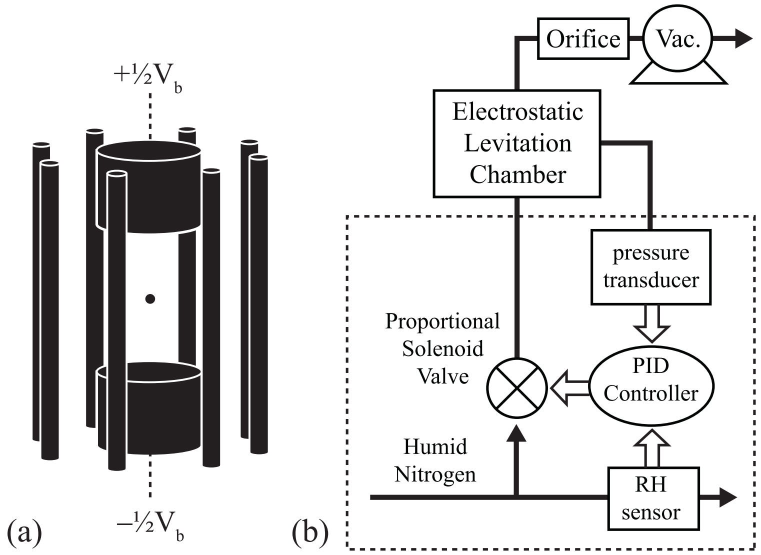

Figure 3.1. (a) Schematic of electrode cage for electrostatic levitation showing particle balanced at the geometric center. (b) Schematic of the environmental control module. The activity of water at the particle is controlled by modulating the pressure of a nitrogen stream containing a fixed mole fraction of water vapor. The levitation chamber, humidifier, and RH sensor are held at constant temperature with recirculating fluid.

droplet, produces a well-defined angular scattering pattern, known as Mie scattering [33], when illuminated by coherent light. The Mie pattern exhibits a series of peaks and valleys in scattered intensity with an angular frequency that increases with diameter. Thus, the observed light scattering pattern (Figure 3.2) provides a measure of the absolute size of the solution droplet. In contrast, an aspherical particle or one with internal heterogeneity produces an irregular light scattering pattern. Therefore, the Mie pattern is lost upon formation of a crystallite in a droplet of supersaturated solution.

All gravimetric data presented below were recorded during a series of experiments using a single charged particle of PEO. The results accord well with measurements made on a number of other particles of the same PEO.

## 3.3 RESULTS

Polyethylene oxide (PEO) exhibits an asymmetric response to humidification as the activity of water within a levitated particle increases and decreases between 0.76 and 0.92 with a scan rate of 0.04 $hr^{-1}$ (Figure 3.3). Starting from a nearly dry solid state, as $a_w$ increases, the particle mass increases by sorption of water into the semicrystalline structure [34] (Zone I, Figure 3.3). As $a_w$ increases further, however, it eventually becomes large enough that the water content increases strongly (Zone II, Figure 3.3), until the water content has reached the vapor-solution isotherm for PEO dissolved in water (Zone III, Figure 3.3).

The transition from sorption into a solid to solution-vapor equilibrium is termed deliquescence. Deliquescence of hygroscopic aerosols governs the formation of liquid droplets in the atmosphere and has been extensively studied for its influence on global climate [35-37]. A

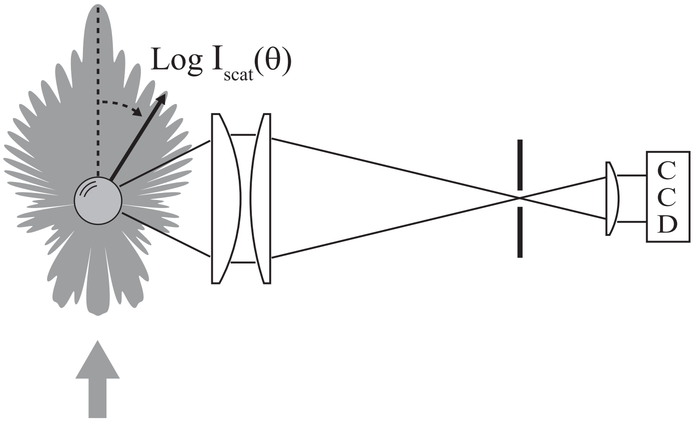

Figure 3.2. Optical configuration for collection of angular light scattering between 78° and 102° relative to the incident laser beam (532 nm, 25 mW). Radiation is focused through an aperature and collimated onto a CCD detector. A logarithmic polar plot of the calculated scattered light intensity as a function of angle for a 5 micron droplet is superimposed.

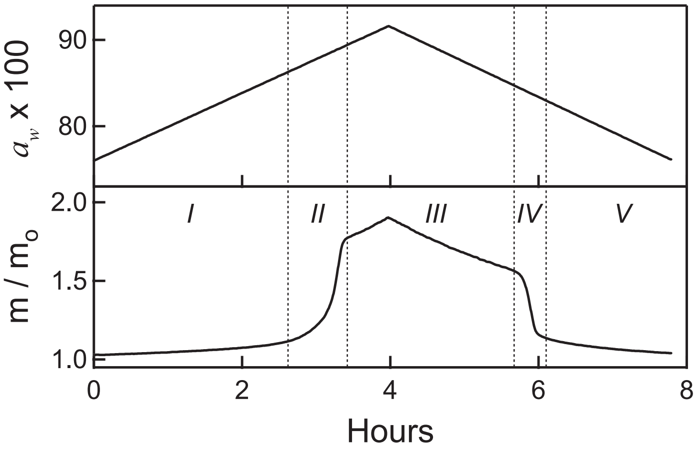

Figure 3.3. Response of the PEO particle to a continuous triangular scan in water activity between 0.76 and 0.92 at 0.04 hr$^{-1}$. Particle mass is normalized by the mass of the dry particle. T = 21.10 ± 0.05 °C.

substance with a well-defined crystal structure, such as a pure inorganic salt, exhibits a simple response to humidification. A sodium chloride particle, for example, absorbs no water with increasing $a_w$ up to the deliquescence point ($a_{w,d}$). The particle then spontaneously dissolves over an extremely narrow range of activity to generate an aqueous solution droplet; salt deliquescence appears graphically as a sharp vertical transition. The PEO particle, in contrast, displays finite water absorption even at low activity, and deliquescence occurs over a relatively wide activity range. This behavior is analogous to that of mixed salt particles, which deliquesce stepwise over a range in activity as the various components activate sequentially [38]. Semicrystalline polymer contains populations of crystallites with varying thickness. Since the free energy of a polymer crystal is a function of lamellar thickness, the thinnest lamellae dissolve at lower water activity than thicker lamellae. The breadth and position of the deliquescence transition therefore reflects the distribution of lamellar thickness within a sample.

At water activity above the deliquescence transition ($a_w > a_{w,d}$), the solution continuously sorbs or evaporates water as $a_w$ increases or decreases along the familiar vapor-liquid isotherm (Zone III, Figure 3.3). Indeed, after dissolving the crystallites, it is possible to continue along the vapor-liquid isotherm into the supersaturated regime by reducing $a_w$ below $a_{w,d}$; hence, the asymmetry in the sorption behavior. During the downward scan, Zone III continues until the solution becomes sufficiently supersaturated that nucleation occurs on the timescale of the experiment. Then propagation of crystallites throughout the particle drives evaporation of water in a process known as efflorescence (Zone IV, Figure 3.3).

Efflorescence, unlike deliquescence, may occur far from equilibrium and is, therefore, ideally probed with single particle techniques. Particle levitation eliminates container surfaces that might catalyze nucleation, and enables isolation of microscopic sample volumes in which highly supersaturated states can be probed; the activity at which a system effloresces ($a_{w,e}$) depends on sample size and purity. Again it is useful to compare the efflorescence observed in the polymer solution to that in a simple salt. For example, decreasing $a_w$ through $a_{w,e}$ in a small drop of supersaturated NaCl solution produces complete expulsion of water over a very narrow range of $a_w$: as soon as a nucleation event occurs, crystal growth rapidly (in effect, instantaneously) incorporates all of the salt. In contrast, PEO crystallization proceeded over a substantial interval of $a_w$, leading to the finite slope in Zone IV (Figure 3.3). The PEO particle also retained residual water after the steep decrease in mass; continued reduction in $a_w$ led to further decrease in the mass (Zone V) as it gradually approached that of the solid during the up scan (Zone I). This "tail" at low activity reflects the slow evolution of crystal morphology characteristic of semicrystalline polymers (secondary crystallization processes) [1, 16-18].

A parametric plot of the recorded mass and water activity clearly illustrates hysteresis between increasing and decreasing scans (Figure 3.4). Representative light scattering patterns confirm the correlation between the sorption/desorption behavior and the dissolution/formation of crystallites (Figure 3.4 A-H). The uniform vertical Mie fringes in images D, E, and F indicate a spherical, optically homogeneous droplet. Images A, B, G, and H each display irregular scattering, a signature of optical heterogeneities or deviations from spherical shape. Image C, of the partially dissolved state, displays distorted Mie fringes indicative of a droplet with only minor surface roughness and/or internal heterogeneity. Comparison of the fringe spacing

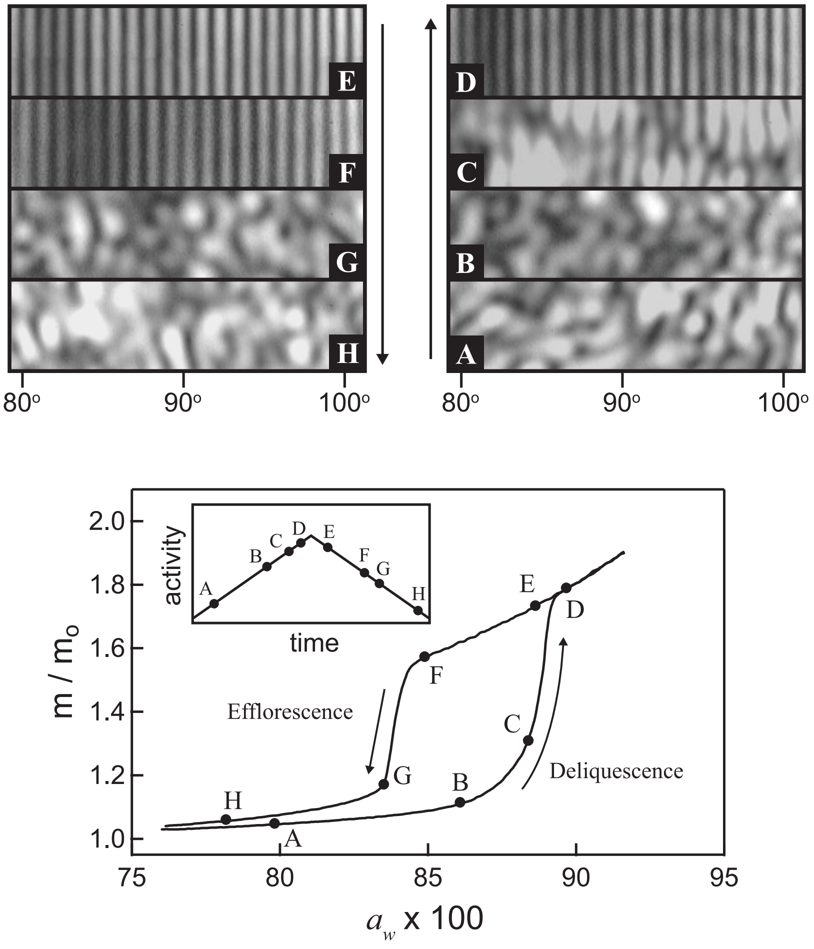

Figure 3.4. Parametric plot (m/m$_o$ vs. $a_w$) of thermodynamic data in Figure 3.3 and images of angular light scattering collected at various times (A – H).

in image D ($m/m_o = 1.8$) with Mie theory indicates a droplet diameter of 33 ± 1 microns, corresponding to a dry PEO mass of 11 ± 1 nanograms.

The presence of crystallites correlates with a negative deviation from the solution isotherm. The most extreme possible decrease in mass corresponds to complete expulsion of water, i.e., dropping to $m_o$. Therefore, an index that increases from 0 to 1 as crystallinity increases may be constructed and applied to the data discussed above (Figure 3.5):

$$I_c(a_w) = \frac{m_{sol}(a_w) - m(a_w)}{m_{sol}(a_w) - m_o} \tag{3.1}$$

where $m_o$ is the mass of the dry PEO particle, $m(a_w)$ is the actual mass of the PEO particle at a given water activity, and $m_{sol}(a_w)$ is the equilibrium mass of the fully dissolved PEO solution droplet at a given water activity; $m_{sol}(a_w)$ is obtained from the final experiment discussed below. The equilibrium water content of the PEO particle depends on the crystal morphology and the hygroscopicity of the various crystalline and noncrystalline domains. The index $I_c$ is a measure of the average hygroscopicity of the particle, normalized by that of the fully dissolved state ($I_c \equiv 0$ on the solution isotherm). PEO crystallinity has been reported to be as high as 85% when measured by calorimetry [39]; although the present index is not expected to correspond precisely to the volume fraction of material that is crystalline, we observe that $I_c$ increases to approximately 90% at the greatest level of crystallinity in our experiments.

The hysteresis in sorption persists even if a substantial population of crystals is deliberately left in the sample at the peak of the scan in $a_w$ (Figure 3.6). The PEO particle was partially dissolved by increasing $a_w$ only to selected values during Scans B ($a_w = 0.892$) and

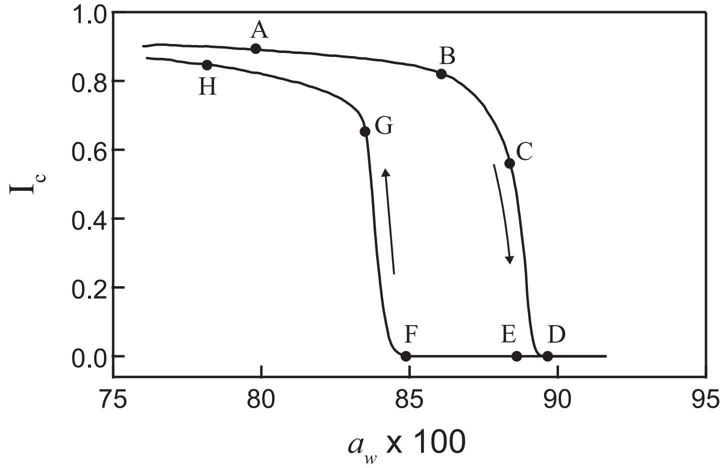

Figure 3.5. $I_c$ vs. $a_w$ for the data in Figures 3.3 and 3.4.

C ($a_w$ = 0.894) before drying. Previous to each of Scans B and C, the particle was brought to the solution state and then re-crystallized with an annealing scan that peaked at $a_w$ = 0.92 (Scans A and A'). The importance of annealing is demonstrated by the deviation of A' from A during deliquescence; the upward shift in $a_{w,d}$ indicates that Scan B caused a shift in the population of lamellae toward thicker crystallites. The deliquescence response during Scans B and C, however, agrees well, indicating similar initial solid state morphologies, since Scans A and A' exhibited identical values of $a_{w.e}$. One unfamiliar with semicrystalline polymers might expect that the residual crystalline material would grow immediately upon drying during Scans B and C. When the activity in the partially solvated particle was decreased, however, $I_c$ remained roughly constant for a time before the particle effloresced, albeit at higher $a_{w,e}$ than for the fully solvated droplets of Scans A and A'. The hysteresis indicates that the rate of secondary nucleation, which is required for crystal growth, is negligible at $a_{w,d}$, but increases with decreasing $a_w$. That $a_{w,e}$ increased clearly indicates that efflorescence was not initiated by homogeneous nucleation; instead the residual crystalline material catalyzed a form of heterogeneous nucleation known as self-nucleation at sufficiently low activity.

The nature of the phase transition in Scans A and A' (Figure 3.6) can be shown by increasing the peak $a_w$ to even higher values. The environmental control module was programmed to ramp the activity of water up and down between 0.76 and 0.95 (dashed curve in Figure 3.7) at a scan rate of 0.04 hr$^{-1}$ immediately following a scan up to $a_w$ = 0.92 (solid curve in Figure 3.7). As $a_w$ decreased, the solution droplet remained metastable well below the activity at which crystallization occurred in the previous scans. The efflorescence observed in Scans A and A' and also in Figure 3.4, therefore, must have been initiated by remnants of lamellae [26-29] that remained after scanning to $a_w$ = 0.92; these remnants appear to have been erased, however,

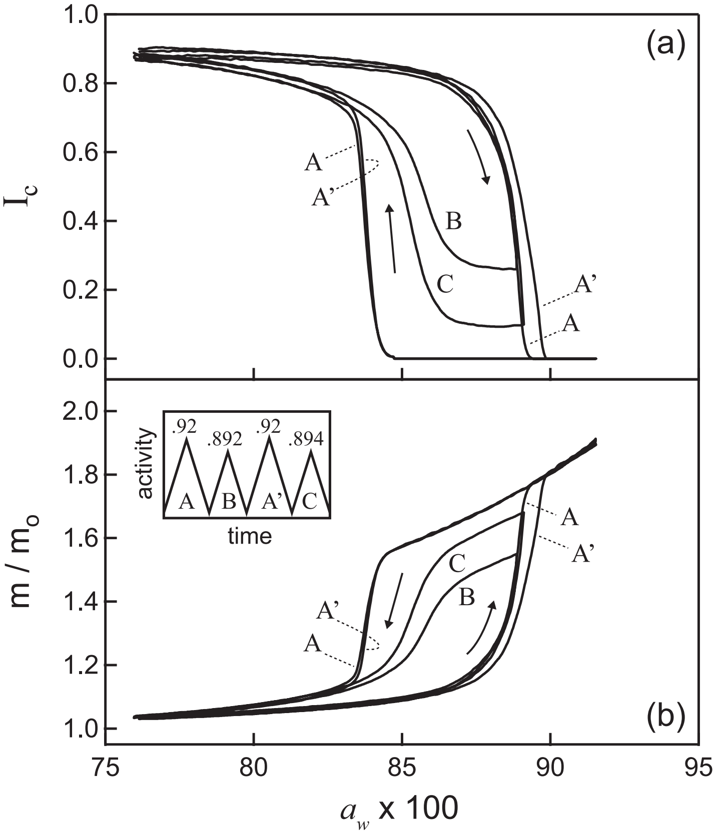

Figure 3.6. (a) $I_c$ vs. $a_w$ and (b) $m/m_o$ vs. $a_w$ for 4 consecutive triangular scans in $a_w$ between 0.76 and 0.92 (A); 0.892 (B); 0.92 (A'); 0.894 (C) at 0.04 $hr^{-1}$. T = 21.10 ± 0.05 °C.

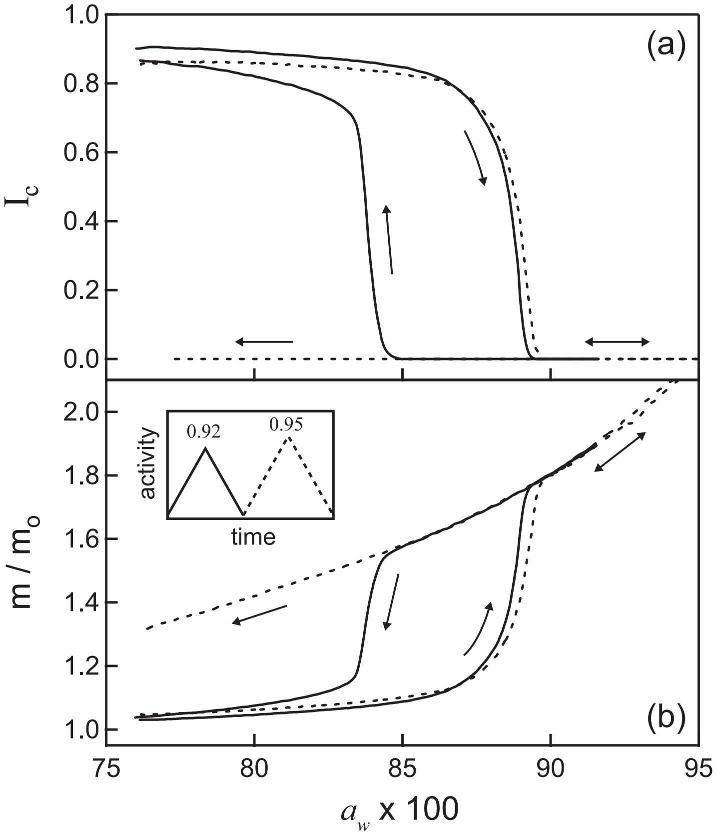

Figure 3.7. (a) $I_c$ vs. $a_w$ and (b) m/m$_o$ vs. $a_w$ for 2 consecutive triangular scans in $a_w$ between 0.76 and 0.92 (solid); 0.95 (dashed) at 0.04 hr$^{-1}$. T = 21.10 ± 0.05 °C.

during a scan up to $a_w = 0.95$. Thus, the nucleation event observed at $a_w = 0.84$ was also not homogeneous, even though the polymer appeared to be fully solvated after a peak activity of $a_w = 0.92$.

## 3.4 DISCUSSION

Our objective here is to illustrate the power of SAGA as a tool to probe thermodynamic and kinetic aspects of polymer crystallization. We begin with analogies to DSC that show how SAGA experiments can be designed and interpreted based on familiar protocols used to study crystallization and melting using calorimetry. We close by highlighting unique experiments that are enabled by SAGA, which are not possible within the limitations of calorimetry.

Those familiar with DSC will immediately recognize that the deliquescence and efflorescence activities ($a_{w,d}$ and $a_{w,e}$) identified by SAGA are analogous to the melting and crystallization temperatures ($T_m$ and $T_x$) of DSC. Each technique observes that phase transitions proceed over a wide range during linear scans in activity or temperature, and each also permits other protocols such as discrete jumps. DSC typically assigns the nominal temperature of a transition to that which exhibits the maximum heat flux. The analogous assignment of nominal activity in our experiments would be that which exhibits the maximum rate of water sorption or evaporation, corresponding to the inflection points in Zones II and IV (Figure 3.3). It should be noted that the heat flux that is monitored by DSC is analogous to the derivative of the mass of sorbed solvent that is monitored by SAGA.

History effects that figure prominently in semicrystalline polymers can be probed by SAGA with protocols reminiscent of those used in calorimetry. Semicrystalline material continuously evolves after primary crystallization to maximize the degree of crystallinity and minimize high-energy fold surfaces. These so-called secondary crystallization processes include thickening of existing lamellae and nucleation and growth of thin platelets in the interlamellar space. DSC detects the consequences of these sluggish processes through changes in the melting behavior after well-defined annealing protocols [17, 18]. Likewise, SAGA can discriminate changes in crystal morphology (e.g., the distribution of lamellar thickness) through shifts in $a_{w,d}$ (cf. Scans A and A', Figure 3.6). Since sorption tracks the transient hygroscopicity, related to the crystalline content, SAGA can readily track gradual evolution of crystallinity over very long times (Zone V, Figure 3.3) that are inaccessible by conventional DSC, which requires relatively rapid changes in crystallinity to generate a measurable heat flow.

Another fascinating history dependence observed in semicrystalline polymers is the "melt memory effect"; even when heated beyond the apparent melting transition, the prior semicrystalline state can influence subsequent crystallization upon cooling. Although the mechanism is not known, the "memory" may arise from small remnants of lamellae that persist above the nominal melting point [26-28] and then serve as athermal nuclei [40] upon cooling. In calorimetry, the effect is manifested after a thermal quench as a shift in the time $\tau$ at which the maximum isothermal crystallization rate is observed. Relative to annealing above the equilibrium melting temperature, $\tau$ increases by an amount that is a function of annealing time and temperature [29]. SAGA displays an analogous "memory effect"; scanning to $a_w = 0.95$ enabled the PEO solution droplet to achieve much greater supersaturation upon drying than did a scan to $a_w = 0.92$ (Figure 3.7). We have also reversed the trend, causing $a_{w,e}$ to systematically increase, by careful selection of a scanning activity protocol; these results are presented in Chapter 3.

SAGA is ideally suited for investigating nucleation kinetics since a single material specimen can be repeatedly probed for statistical analysis [32, 41-43]. Elimination of container surfaces that might catalyze nucleation and isolation of microscopic sample volumes allow access to highly supersaturated states. Electrostatic levitation has been successfully implemented with sample mass ranging from less than a picogram [44] ($D_p$ < 1 micron) to greater than a milligram [45] ($D_p$ > 1 millimeter), although not with identical instruments. Since only a single nucleation event is required to crystallize an entire sample, SAGA thus has the potential to probe at least 9 orders of magnitude in nucleation rate (i.e., events per unit volume per unit time) with experiments performed on similar timescales; extending measurement times will further enhance the dynamic range.

The most obvious departure from DSC is that SAGA directly controls the chemical potential under isothermal conditions. Polymer crystallization and dissolution proceed without simultaneous changes in the enthalpy of fusion that accompany studies of polymer crystallization from the melt or traditional studies of polymer crystallization from solution, which control the temperature at fixed (and usually very dilute) concentration [46]. The small surface-to-volume ratio of levitated particles facilitates uniform changes in the concentration of sorbed solvent that would take prohibitive time to equilibrate in bulk samples. SAGA, therefore, offers an opportunity to study the physics of polymer crystallization in unique systems, namely highly concentrated solutions.

# REFERENCES

1 G. R. Strobl, *The Physics of Polymers: Concepts for Understanding their Structures and Behavior* (Springer-Verlag, Berlin, 1996).

2 S. Z. D. Cheng, A. Keller, *Annu. Rev. Mater. Sci.* 28, 533 (1998).

3 J. D. Hoffman, G. T. Davis, J. I. Lauitzen Jr., *The rate of crystallization of linear polymers with chain folding. In Treatise on solid state chemistry*, N. B. Hannay, Ed., (Plenum, New York, 1976) vol. 3, ch. 7, 497-614.

4 S. Z. D. Cheng, B. Lotz, *Polymer* 46, 8662 (2005).

5 B. Wunderlich, A. J. Mehta, *Polymer. Sci.* B 2, 255 (1974).

6 W. Banks, M. Gordon, A. Sharples, *Polymer* 4, 289 (1963).

7 E. J. Davis, *Aer. Sci. Tech.* 26, 212 (1997).

8 R. L. Cormia, F. P. Price, D. Turnbull, *J. Chem. Phys.* 37, 1333 (1962).

9 J. A. Koutsky, A. G. Walton, E. J. Baer, *J. App. Phys.* 38, 1832 (1967).

10 M. L. Arnal, M. E. Matos, R. A. Morales, O. O. Santana, A. J. Müller, *Macromol. Chem. Phys.* 199, 2275 (1998).

11 Y.-L. Loo, R. A. Register, A. J. Ryan, *Phys. Rev. Let.* 84, 4120 (2000).

12 M. V. Massa, J. L. Carvalho, K. Dalnoki-Veress, *Eur. Phys. J. E* 12, 111 (2003).

13 G. C. Alfonso, T. P. Russell, *Macromolecules* 19, 1143 (1986).

14 B. Fillon, J. C. Wittman, B. Lotz, A. J. Thierry, *Polymer Sci.* 31, 1383 (1993).

15 I. Okazaki, B. Wunderlich, *Macromolecules* 30, 1758 (1997).

16 Z.-G. Wang, B. S. Hsiao, B. B. Sauer, W. G. Kampert, *Polymer* 40, 4615 (1999).

17 A. Alizadeh, L. Richardson, L. Xu, S. McCartney, H. Marand, Y. W. Cheung, S. Chum,

*Macromolecules* 32, 6221 (1999).

18 H. Marand, Z. Huang, *Macromolecules* 37, 6492 (2004).

19 M. Imai, K. Mori, T. Mizukami, T. Kanaya, *Polymer* 33, 4451 (1992).

20 N. J. Terrill, P. A. Fairclough, E. Towns-Andrews, B. U. Komanschek, R. J. Young, A. J. Ryan, *Polymer* 39, 2381 (1998).

21 G. Kumaraswamy, A. M. Issaian, J. A. Kornfield, *Macromolecules* 32, 7537 (1999).

22 B. Fillon, A. Thierry, B. Lotz, J. C. Wittman, *J. Therm. Analysis* 42, 721 (1994).

23 T. Bauer, R. Thomann, R. Mülhaupt, *Macromolecules* 31, 7651 (1998).

24 K. Nagarajan, K. Levon, A. S. Myerson, *J. Therm. Analysis* 59, 497 (2000).

25 K. N. Krüger, H. G. Zachmann, *Macromolecules* 26, 5202 (1993).

26 H. Janeschitz-Kriegl, *Col. Polym. Sci.* 275, 1121 (1997).

27 H. Janeschitz-Kriegl, E. Ratajski, H. Wippel, *Col. Polym. Sci.* 277, 217 (1999).

28 H. Janeschitz-Kriegl, *Col. Polym. Sci.* 281, 1157 (2003).

29 G. C. Alfonso, A. Ziabicki, *Col. Polym. Sci.* 273, 317 (1995).

30 A. Häfele, B. Heck, T. Hippler, T. Kawai, P. Kohn, G. Strobl, *Eur. Phys. J. E* 16, 217 (2005).

31 M. V. Massa, M. S. M. Lee, K. Dalnoki-Veress, *J. Polymer Sci.* B 43, 3438 (2005).

32 Chapter 2 of this thesis.

33 H. C. van de Hulst, *Light Scattering by Small Particles* (Wiley, New York, 1957).

34 N. S. Murthy, M. K. Akkapeddi, W. J. Orts, *Macromolecules* 31, 142 (1998).

35 C. B. Richardson, J. F. Spann, *J. Aer. Sci.* 15, 563 (1984).

36 I. N. Tang, H. R. Munkelwitz, *J. Col. Int. Sci.* 98, 430 (1984).

37 M. D. Cohen, R. C. Flagan, J. H. Seinfeld, *J. Phys. Chem.* 91, 4563 (1987).

38 I. N. Tang, H. R. Munkelwitz, J. G. Davis, *J. Aer. Sci.* 9, 505 (1978).

39 L. B. Yang, G. Venkatesh, R. Fassihi, *J. Pharm. Sci.* 85, 1085 (1996).

40 J. C. Fischer, J. H. Hollman, D. Turnbull, *J. Appl. Phys.* 19, 775 (1948).

41 D. Knezic, J. Zaccaro, A. S. Myerson, *J. Phys. Chem. B* 108, 10672 (2004).

42 M. A. Hamza, B. Berge, W. Mikosch, E. Rühl, *Phys. Chem. Chem. Phys.* 6, 3484 (2004).

43 B. Krämer, O. Hübner, H. Vortisch, L. Wöste, T. Leisner, M. Schwell, E. Rühl, H. Baumgärtel, *J. Chem. Phys.* 111, 6521 (1999).

44 S. Schlemmer, J. Illemann, S. Wellert, D. Gerlich, *J. Appl. Phys.* 90, 5410 (2001).

45 W. K. Rhim, S. K. Chung, D. Barber, K. F. Man, G. Gutt, A. Rulison, R. E. Spjut, *Rev. Sci. Instrum.* 64, 2961 (1993).

46 D. J. Blundell, A. Keller, A. J. Kovacs, *J. Polymer Sci. B - Poly. Let.* 4, 481 (1966).

*Chapter 4*

# MANIPULATION OF ATHERMAL NUCLEI IN AQUEOUS POLYETHYLENE OXIDE SOLUTION

## 4.1 INTRODUCTION

Polymers crystallize to form metastable chain-folded platelets called lamellae, rather than extended-chain crystals, because of kinetic limitations [1]. Lamellae have very large surface-to-volume ratio and, therefore, must grow far from equilibrium, where the bulk free energy gain is sufficient to overcome the cost of the high energy fold surface. Since crystallization is an activated process, lamellae emerge with a thickness that is greater than the marginally stable thickness at the growth conditions, and so hysteresis is always observed between crystallization and dissolution or melting. After primary crystallization, crystallinity often increases further over long times as a result of sluggish secondary processes such as interlamellar crystallization [2] and thickening of pre-existing lamellae [3, 4].

Memory effects in semicrystalline polymers have been documented for a variety of systems in which the rate of crystallization depends on the temperature and duration of a prior melting step [5-13]. This phenomenon is usually attributed to small remnants of the crystalline phase that persist for long times above the apparent melting temperature and then serve as athermal nuclei [14] upon cooling. Although many believe that remnants survive exclusively because of sluggish kinetics [9-13, 15], thermodynamic considerations may also play an important role [16-18].

We previously introduced scanning activity gravimetric analysis (SAGA) as a novel technique for investigating polymer crystallization from concentrated polymer solution under isothermal conditions [19]. This chapter reports memory effects observed by SAGA in aqueous polyethylene oxide. The present results suggest that small remnants of lamellae persist beyond the apparent dissolution point. At water activities above the value that dissolves all detectable lamellae, the remnants gradually evolve toward increasing or decreasing thickness in response to certain processing protocols, as indicated by a shift in the conditions at which they catalyze crystal growth when the concentration of the polymer solution is subsequently increased. A simple model describing the free energy of a lamellar crystal based on insights of Janeschitz-Kriegl [16-18] captures the metastability of lamellar remnants and their evolution in thickness. The qualitative successes of the model lend support to the thermodynamic rationalization of memory effects in semicrystalline polymers.

## 4.2 EXPERIMENTAL

An automated single particle electrostatic levitation system, described in detail elsewhere [20], was used to perform scanning activity gravimetric analysis (SAGA) on PEO (Sigma Aldrich Co.; Mw = 100,000 g/mol), scanning the activity of water. A three-dimensional electrostatic field generated by a cage of electrodes (Figure 4.1a) suspends a micron-sized charged particle against gravitational, aerodynamic, and Brownian forces; the DC balancing voltage ($V_b$) applied across the disk electrodes shown in Figure 4.1a is proportional to mass. Automated position control maintains the particle within a finite view volume defined by an illuminating laser beam. The balancing voltage is continuously recorded as the sorbed water content equilibrates with the humid atmosphere during an experiment. The relative mass ($m/m_o$) is

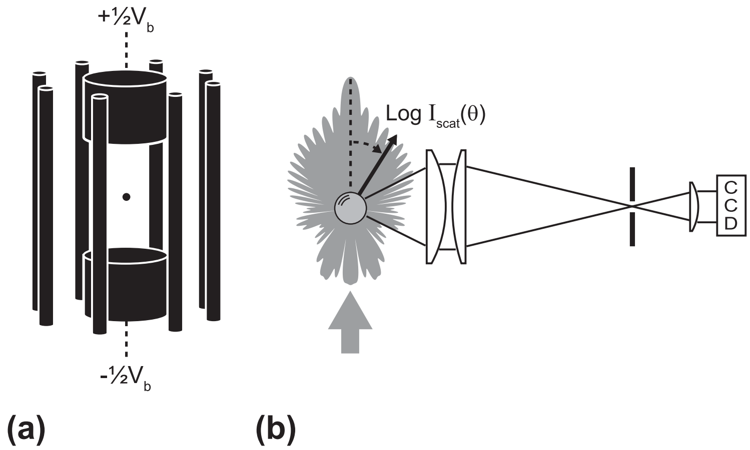

Figure 4.1. (a) A single charged particle is levitated using electrostatic forces that can be dynamically adjusted using an electrode cage to hold the particle at the geometric center in the environmental control chamber that imposes a programmed history of conditions of water activity (relative humidity) and temperature. A laser beam (532 nm, 25 mW) is incident on the particle and the scattered intensity is observed over a selected angular range. (b) View down the central axis of the electrode cage illustrates the angular range (78° to 102° relative to the incident laser beam) over which the scattered intensity is monitored. Radiation is focused through an aperature and collimated onto a CCD detector. The schematic shows the Mie pattern of scattered light intensity calculated for a 5 micron droplet illustrated as a logarithmic polar plot of the intensity as a function of angle.

calculated by normalizing the instantaneous balancing voltage by the balancing voltage in the dry state, i.e., $m/m_o = V_b/V_{b,dry}$. The relative humidity, or equivalently the water activity $a_w$, and temperature of a nitrogen atmosphere surrounding the particle are strictly regulated by an environmental control module. The apparatus can be programmed to impose any desired water activity history; the experiments described below use simple constant rate scans and steps.

Dissolution and crystallization are directly observed through changes in sorbed water content and optical properties. When all crystallites dissolve, the sample becomes a spherical droplet of polymer solution. A micron-sized optically homogeneous sphere, such as a small solution droplet, produces a well-defined angular scattering pattern when illuminated by coherent light. This Mie pattern [21] exhibits a series of peaks and valleys in scattered intensity (Figure 4.1b). The angular frequency of the pattern increases with diameter, providing a measure of the absolute size of the solution droplet. In contrast, an aspherical particle, or one with internal heterogeneity, produces an irregular light scattering pattern. The Mie pattern is, therefore, lost upon formation of a crystallite in a droplet of supersaturated solution.

Gravimetric data presented below were recorded during experiments using three different particles of PEO taken from the same batch of material, distinguished as PEO-1, PEO-2, and PEO-3. Each particle has a mass of several nanograms, so it is possible that variations in composition that might not be evident macroscopically, could cause differences among different ~10 ng samples of a given material. Therefore, it is significant that the results on these three distinct particles accord well with each other and with measurements made on a number of other particles of the same PEO.

## 4.3 RESULTS

The response of PEO-1 to varying water activity ($a_w$) was recorded continuously for 70 hours (Figure 4.2). The activity of water vapor surrounding the particle was programmed to alternately decrease and increase at a constant scan rate of 0.05 $\text{hr}^{-1}$ at 20.25 ± 0.05 °C. Each cycle is assigned a letter and the increasing half of the scan is indicated by a prime (e.g., A/A'). The minimum value of each cycle was held constant at $a_{w,min} = 0.72$. The peak value was $a_{w,max} = 0.92$ for the first set of scans (A' – F') and increased to $a_{w,max} = 0.95$ for two subsequent scans (G' and H').

As $a_w$ increased during each primed scan (e.g., A'), the PEO particle at first sorbed little water vapor and exhibited uncorrelated light scattering since the sample remained highly crystalline (Figure 4.3). At sufficiently high $a_w$, however, the thinnest lamellae in the crystallite population began to dissolve and the water sorption increased more strongly with increasing $a_w$. Further increase in $a_w$ eventually dissolved the entire population, signified by a sharp decrease in the rate of water sorption and the emergence of Mie scattering; the semicrystalline PEO particle had "deliquesced" and become a spherical aqueous solution droplet. Reducing $a_w$ during Scan B decreased the water content to create an increasingly concentrated solution. As the droplet evaporated water, the reduction in volume was accompanied by a decrease in the number of fringes observed in the angular light scattering pattern. Using Mie theory to infer the droplet volume and using the density of water, the balancing voltage can be converted to mass, revealing that the dry particle has mass of 11 ± 1 nanograms. As $a_w$ was decreased the solution eventually became sufficiently supersaturated that nucleation occurred and crystalline lamellae propagated throughout the particle, driving the evaporation of water and disrupting the light scattering pattern during a process known as "efflorescence". A parametric plot of the

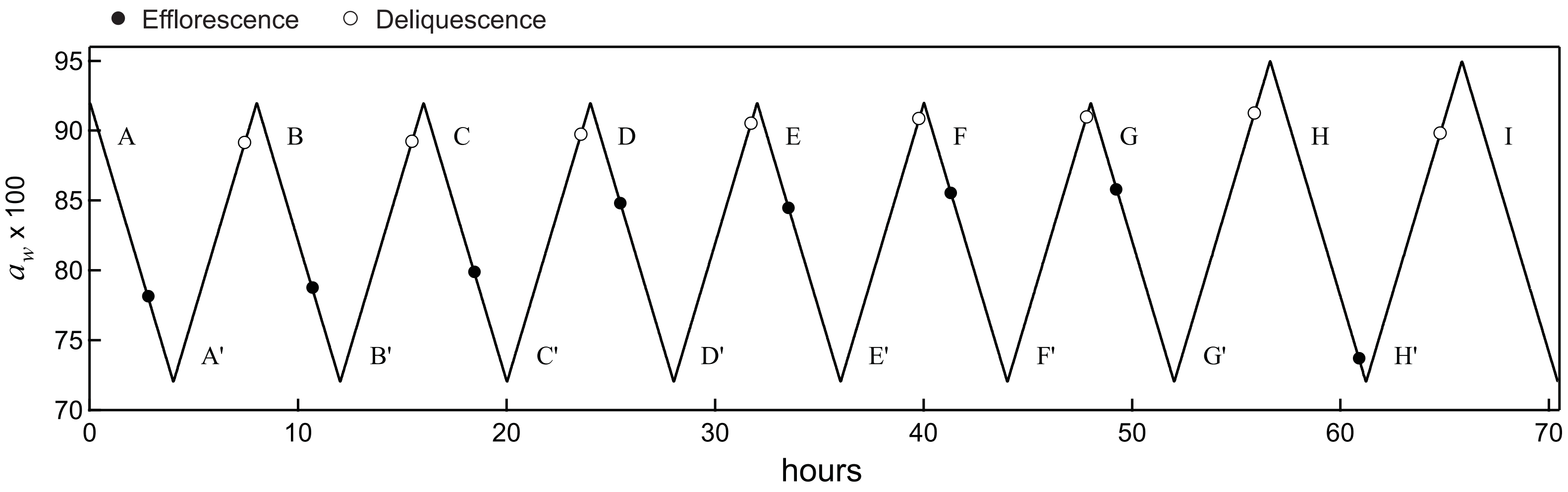

Figure 4.2. Response of PEO-1 to repeated continuous triangular scans in water activity between 0.72 and 0.92 (A – G) and between 0.72 and 0.95 (G' – I) at 0.05 $hr^{-1}$ under isothermal conditions (T = 20.25 ± 0.05 °C). During each downward scan, the water activity at which a dramatic decrease in mass due to crystallization (efflorescence transition) occurred is indicated by a filled circle. During each upward scan, the water activity at which an abrupt increase in mass due to dissolution (deliquescence transition) occurred is indicated by an open circles.

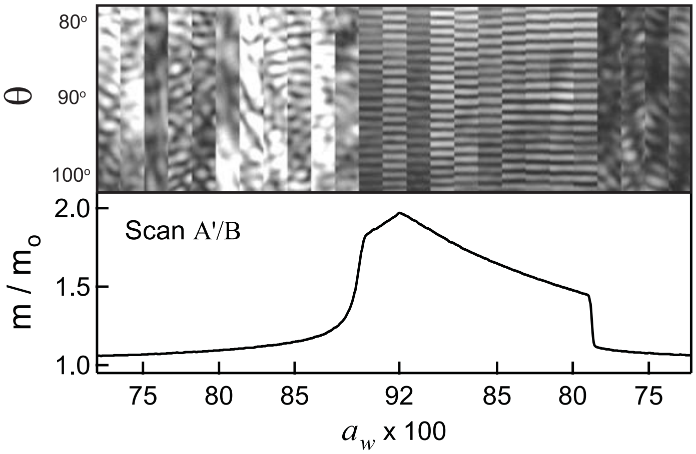

Figure 4.3. Light scattering pattern (captured at 20 minute intervals) and normalized particle mass m/m$_o$ (recorded at 20 second intervals) as functions of water activity $a_w$ during upward scan A' and downward scan B of Figure 4.2. The $a_w$ axis also corresponds to a linear increase in time (8 hours total). The particle begins in a semicrystalline solid state with a small amount of sorbed water. When $a_w$ reaches approximately 0.9, the mass increases strongly and the image of the angular light scattering indicates that an optically homogeneous spherical solution droplet forms. From this transition onward to the peak $a_{w,max}$ and down to $a_w$ approximately 0.8, the water content of the sample follows the solution isotherm for the PEO/water system. The transition from semicrystalline sorption behavior to solution sorption behavior is the deliquescence transition. The reverse transition from the solution to the semicrystalline state, known as efflorescence, is marked by the disappearance of the Mie pattern and an abrupt decrease in mass.

recorded mass as a function of $a_w$ clearly illustrates hysteresis between dissolution and crystallization (Figure 4.4a). The index $I_c$ that is plotted in Figure 4.4b increases from 0 in the fully dissolved solution to 1 as crystallinity increases. It is defined as

$$I_c(a_w) = \frac{m_{sol}(a_w) - m(a_w)}{m_{sol}(a_w) - m_o}, \tag{4.1}$$

where $m_o$ is the mass of the dry PEO particle, $m(a_w)$ is the actual mass of the PEO particle at a given water activity, and $m_{sol}(a_w)$ is the equilibrium mass of the fully dissolved PEO solution droplet at a given water activity.

Since a single efflorescence or deliquescence event occurs over a range in activity (Figures 4.3 and 4.4), the nominal activity for each transition ($a_{w,e}$ or $a_{w,d}$) is defined as the activity at which the maximum rate of change in sorbed water is observed. As the activity repeatedly scanned up and down between $a_w = 0.72$ and 0.92 (Scans A/A' – G/G'), both $a_{w,e}$ and $a_{w,d}$ systematically increased (Figure 4.2). After the activity increased to $a_w = 0.95$ during Scans G' and H', however, both $a_{w,e}$ and $a_{w,d}$ systematically decreased.

The coupling between the changes in $a_{w,e}$ and $a_{w,d}$ can be understood by considering the way the dissolution (deliquescence transition) during an upward scan depends upon the population of lamellae that formed during crystallization (efflorescence transition) in the preceding downward scan. For example, the populations of lamellae that deliquesced during Scans A' and E' were created during Scans A ($a_{w,e} \approx 0.78$) and E ($a_{w,e} \approx 0.86$) respectively. Since lower $a_{w,e}$ results in a thinner population of lamellae that is less stable, $a_{w,d}$ was smaller during Scan A' ($a_{w,d} \approx 0.89$) than during Scan E' ($a_{w,d} \approx 0.91$).

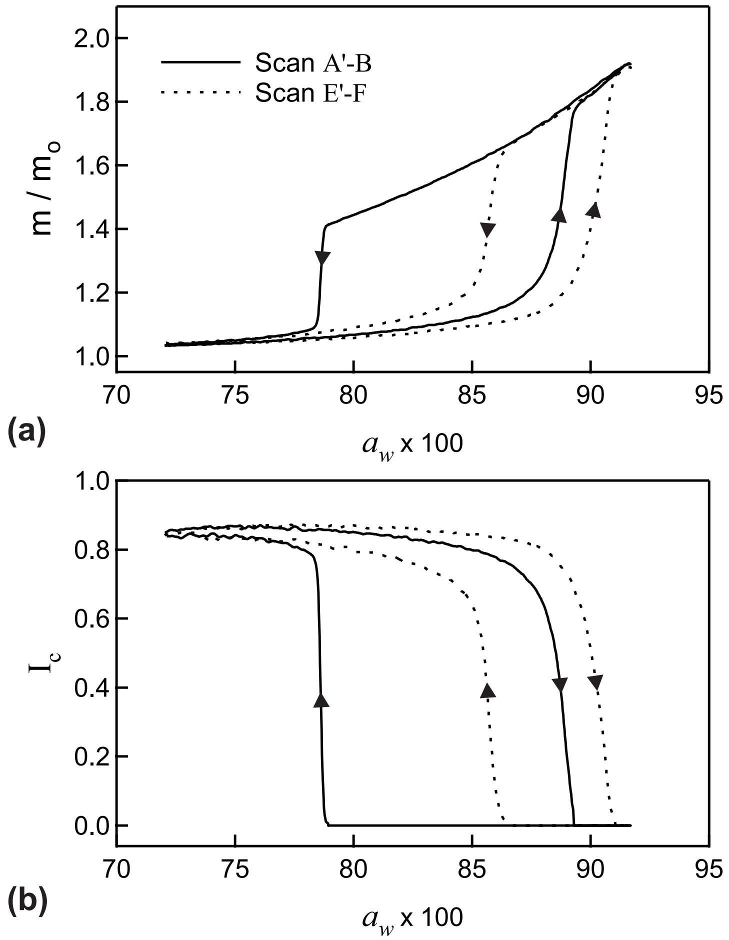

Figure 4.4. (a) $m/m_o$ vs. $a_w$ and (b) $I_c$ vs. $a_w$ for Scans A'/B (solid curve) and E'/F (dashed curve) of Figure 4.2.

Throughout the sequence of scans between $a_w$ = 0.72 and 0.92, $a_{w,d}$ increased linearly with increasing $a_{w,e}$ (Figure 4.5). This relationship between $a_{w,d}$ and $a_{w,e}$ is analogous to that observed between the crystallization temperature $T_x$ and the melting temperature $T_m$ during differential scanning calorimetry (DSC) experiments; lamellae grow thinner at deeper supersaturation (or subcooling) and, therefore, deliquesce (or melt) at more modest conditions. The equilibrium melting temperature $T_m^o$ of the hypothetical infinite extended-chain polymer crystal has been estimated by the intersection of the extrapolated linear dependence of $T_m$ on $T_x$ and the equilibrium line $T_m = T_x$ (the so-called Hoffman-Weeks linear extrapolation) [1]. Analogous extrapolation of the dependence of $a_{w,d}$ on $a_{w,e}$ yields an estimated equilibrium deliquescence activity $a_{w,d}^o$ of 0.928. In light of recent refinements to the classical Hoffman-Weeks extrapolation [22], this simple analysis likely underestimates $a_{w,d}^o$, but it does strongly suggest that the scans in Figure 4.2 that peaked at $a_w$ = 0.92 remained below $a_{w,d}^o$ throughout, while those that peaked at $a_w$ = 0.95 annealed the sample above $a_{w,d}^o$ for some time.

Another interesting coupling is observed in the efflorescence transition; the greater the water activity (i.e., the lower the supersaturation) at which the onset of crystallization occurs, the broader the efflorescence transition (Figure 4.4). Compare Scans A'/B and E'/F, for example; in Scan B, $a_{w,e}$ is lower and the transition is sharper than in Scan F. Growth at higher $a_w$ favors thicker lamellae, which perhaps do not fill space as densely as their thinner counterparts, since primary crystallization was not as complete during Scan F as during Scan B (Figure 4.4b). The gradual expulsion of water as $a_w$ decreased from 0.85 to 0.72 during Scan F suggests that further enhancement of crystallinity results from secondary processes (likely interlamellar crystallization) [2] that were not required during Scan B.

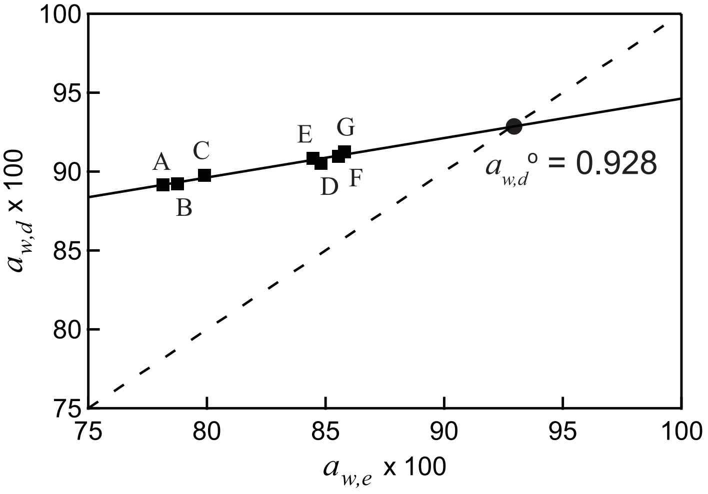

Figure 4.5. $a_{w,d}$ vs. $a_{w,e}$ for 7 consecutive Scans (A/A' – G/G') indicating a positive correlation between $a_{w,d}$ and the preceeding $a_{w,e}$. A Hoffman-Weeks extrapolation extimates the equilibrium deliquescence activity of PEO ($a_{w,d}^{o}$ = 0.928 at T = 20.25 °C), which describes the stability of the hypothetical infinite extended-chain crystal.

The response of PEO-2 to a programmed activity scan (at constant T = 21.10 ± 0.05 °C) demonstrates gradual formation of a population of particularly stable lamellae over 12 hours at constant activity in a partially dissolved state (Figure 4.6). Prior to this experiment, the PEO-2 solution droplet did not crystallize as $a_w$ ramped down from 0.92 to 0.50 at 0.04 $hr^{-1}$. The solution droplet was then rapidly quenched from $a_w = 0.50$ to $a_w = 0$ (still isothermal at T = 21.10 ± 0.05 °C), causing it to crystallize (indicated by an abrupt change in the light scattering pattern). After 30 minutes at $a_w = 0$, the activity was stepped up to $a_w = 0.70$ and held for 5 minutes to allow equilibration. The activity then ramped up from $a_w = 0.70$ to 0.88 at 0.04 $hr^{-1}$ and held at $a_w = 0.88$ for 12 hours ($t_1$ to $t_2$ in Figure 4.6a) before continuing to increase to $a_w = 0.92$ at 0.04 $hr^{-1}$. PEO-2 was partially dissolved at $t_1$, and the crystallinity slowly increased at constant $a_w = 0.88$, manifested by the gradual expulsion of water ($m/m_o$ decreased 0.19 by $t_2$); this annealing step appears as a vertical decrease in mass in Figure 4.6b and a vertical increase in $I_c$ in Figure 4.6c. As $a_w$ then increased further, the remaining crystals dissolved to produce an aqueous solution droplet. The deliquescence after annealing, however, was shifted to greater $a_w$ compared to the deliquescence that would have been observed without annealing (dotted line, Figure 4.6c inset).

The response of PEO-3 to step changes in activity from the dry to the partially dissolved state exhibits rapid dissolution of the lamellae that are not stable at the increased $a_w$ (within approximately 30 minutes) followed by gradual formation of more stable lamellae (Figure 4.7). Duplicate experiments (Trials i and ii) were annealed at $a_w = 0.88$ after crystallization during a quench to $a_w = 0$ (the particle was allowed to crystallize at $a_w = 0$ for 10 minutes). Trial iii was annealed at the same $a_w = 0.88$ after crystallization at a less severe supersaturation (a quench to $a_w = 0.70$ for 10 minutes). Since crystallization occurred at higher activity for Trial iii, the

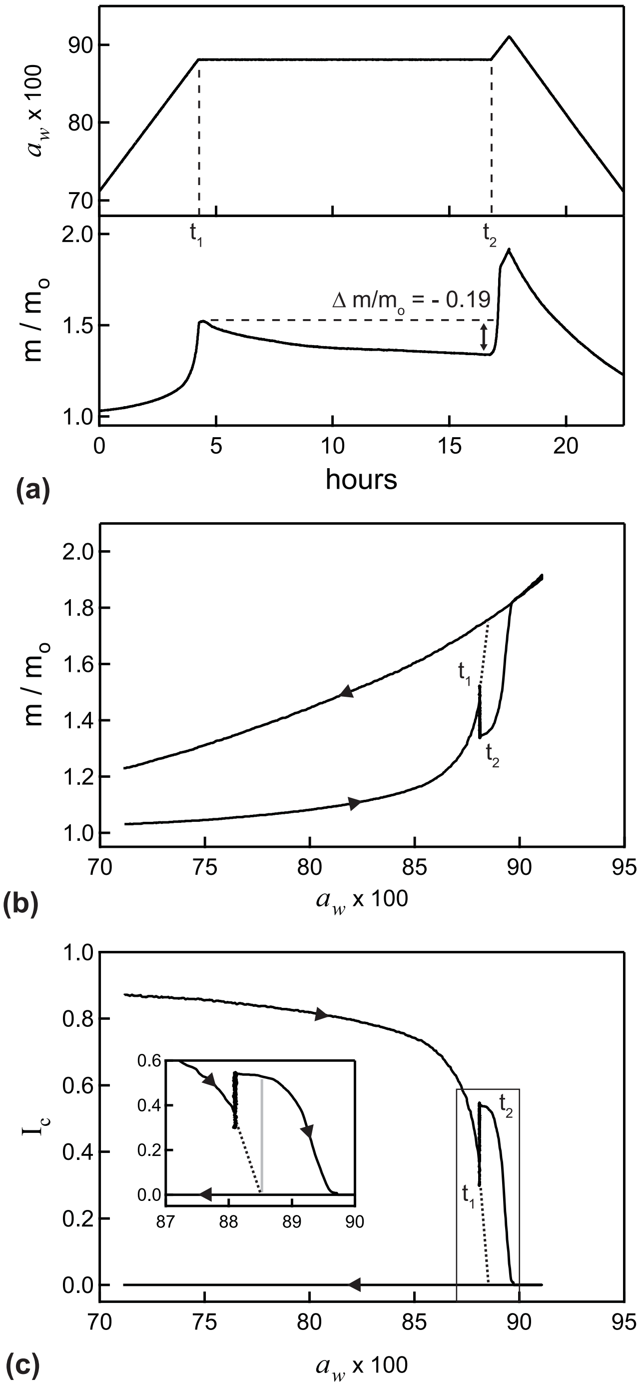

Figure 4.6. (a) Response of PEO-2 to a continuous triangular scan in water activity between 0.72 and 0.92 at 0.04 $hr^{-1}$ that paused at $a_w$ = 0.88 for 12 hours (from $t_1$ to $t_2$). (b) $m/m_o$ vs. $a_w$ and (c) $I_c$ vs. $a_w$ indicate an increase in $a_{w,d}$ after the annealing time. T = 21.10 ± 0.05 °C.

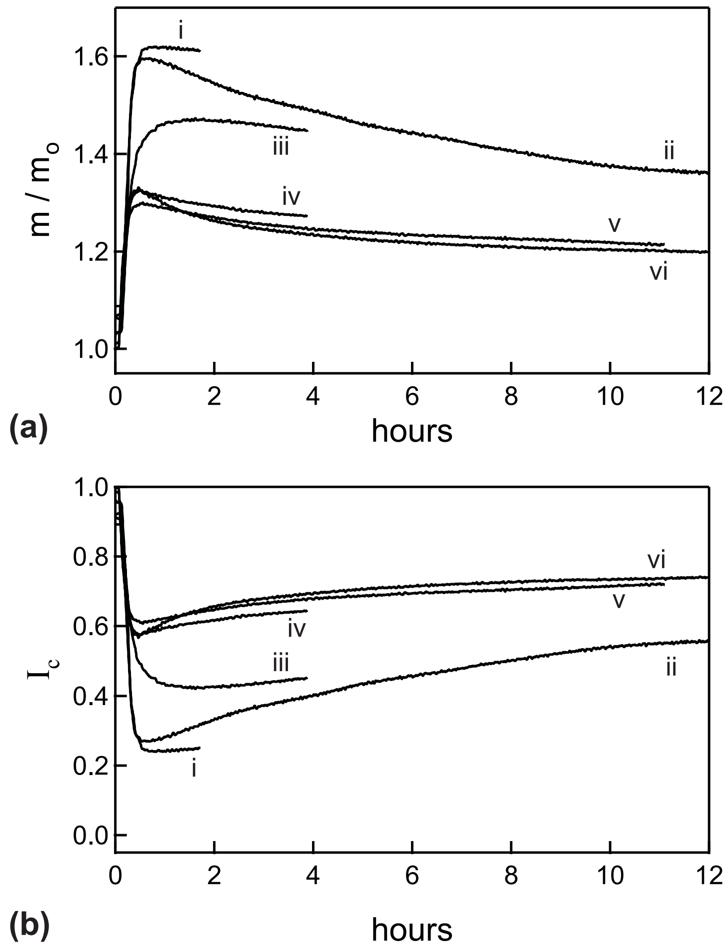

Figure 4.7. (a) $m/m_o$ and (b) $I_c$ for PEO-3 in response to step changes from the dry semicrystalline state at $a_w = 0$ to the partially dissolved state at $a_w = 0.88$ (i, ii, and iii) and 0.87 (iv, v, and vi). T = 21.10 ± 0.05 °C.

sample contained a thicker population of lamellae, and, therefore, initially dissolved to a lesser extent at $a_w = 0.88$ than did Trials i and ii. Triplicate experiments (iv, v, and vi) were annealed at $a_w = 0.87$ after crystallization during a quench to $a_w = 0$ for 10 minutes. In all cases, the initial dissolution in response to the jump in water activity is rapid. For samples that have the same solid state history, the jump to $a_w = 0.88$ (i and ii) dissolved a greater fraction of the lamellar population than a jump to $a_w = 0.87$ (iv, v and vi). For samples jumped to the same elevated activity, those crystallized rapidly at a deep supersaturation (i and ii) have a greater fraction of unstable lamellae that immediately dissolve relative to the population that forms during slow growth and mild supersaturation (iii). In all cases, subsequent increase in crystallinity was very slow.

## 4.4 DISCUSSION

Our interpretation of these results is organized as follows. First, the above observations indicate that crystalline remnants after dissolution of the solid state persist at activities substantially beyond that which dissolves all detectable lamellae. Analogous to memory effects observed in the melt, these remnants persist up to the equilibrium deliquescence activity $a_{w,d}^o$, just as the melt memory effect persists up to the equilibrium melting temperature $T_m^o$. Second, we argue that the strong asymmetry in kinetics between lateral growth or dissolution and lamellar thickening governs the dissolution trajectory of a lamella and, hence, the geometry of the remnant it may leave behind. Finally, we offer an integrated thermodynamic/kinetic perspective that is capable of describing the existence and evolution of athermal nuclei. In accord with the ideas of Janeschitz-Kriegl [16-18], we show that a model of interfacial energy of the fold surface that reflects the reduced constraints near the perimeter of a lamella captures the observed behavior (in contrast, the conventional treatment of the surface energy of fold surface as uniform does not).

### 4.4.1 Existence and Persistence of Crystal Remnants

Systematic manipulation of $a_{w,e}$ (Figure 4.2) indicates that crystallizations that occurred during these efflorescence events in aqueous PEO are not initiated by homogeneous thermal nucleation, which would exhibit random variation about some average $a_{w,e}$ with repeated experiments [20]. We believe instead that crystallization is catalyzed by persistent remnants of dissolved lamellae, which serve as athermal nuclei. If these remnants are clusters containing a small number of molecular segments and folds, the cluster length would correlate with the conditions at which a cluster initiates lateral crystal growth, i.e., clusters of decreasing length should require a greater supersaturation to become "awake". Consequently, the systematic increase (or decrease) in $a_{w,e}$ during repeated scans to $a_w$ = 0.92 (or 0.95) indicates that the population of athermal nuclei in solution shifts to decreased (or increased) length in response to certain processing histories.

These clusters must be sufficiently small that they do not affect Mie scattering, so they are submicron sized. They can also persist for hours while the humidity is above the value that causes lamellar crystals to dissolve ($a_{w,d}$). In Figure 4.2, for example, the elapsed time from the completion of deliquescence to the time that $a_w$ returns to that value during the subsequent downward scan is approximately 2 hours. These clusters must, therefore, have an exemption from the physics that drives chains to dissolve from edges of large lamellae since, following a sudden jump up to $a_w$ = 0.88, the dissolution of lamellae that are unstable at this condition is complete in less than 30 minutes (Figure 4.7). If in the solid state lamellae have radius 10 microns or more, the velocity of the dissolution front must be 0.3 microns per minute or more, yet the submicron size clusters persist for hours at significantly greater $a_w$. The persistence and evolution of the remnants, therefore, cannot be attributed exclusively to sluggish dissolution kinetics; thermodynamic considerations are required to rationalize their long lifetime.

### 4.4.2 Kinetic Considerations in Formation of Crystal Remnants

In accord with prior literature, the results above show that the rate at which lamellae increase in radius during efflorescence (Figures 4.3 and 4.4) is significantly greater than the rate of lamellar thickening (Figures 4.6 and 4.7) [3, 4]. Although it is not possible to quantify the rate of thickening during prolonged annealing at a partially deliquesced state (Figure 4.7), we can confirm that thickening has occurred from the shape of the subsequent deliquescence (Figure 4.6). Of the population of lamellae surviving at time $t_1$, all detectable lamellae would have been dissolved at approximately $a_w = 0.885$ if the upward ramp were simply continued. Instead, following the 12 hour annealing time, negligible dissolution occurred in the interval $0.880 < a_w < 0.885$ during the deliquescence. The population of lamellae present at $t_1$, therefore, transformed to a population of thicker lamellae either by thickening or dissolving and then growing onto thicker crystals. Thickening is more likely in our opinion, since the dissolution was complete on a relatively short timescale after the jump to $a_w = 0.880$. We infer that thickening occurs on a timescale of approximately 10 hours. Some of the increase in crystallinity during annealing may also occur by lateral growth of thick lamellae (also a very slow process). In the following discussion we combine insight into the thermodynamic driving forces for changes in radius and thickness with the extreme asymmetry in the kinetics of lateral addition and thickening.

### 4.4.3 Integrated Thermodynamic/Kinetic Perspective

As a point of departure for modeling the free energy of small clusters, consider classical nucleation theory for a droplet of pure liquid nucleating from a supersaturated vapor [23, 24]. The change in free energy of the system upon formation of a condensed cluster is approximated as the sum of the energy increase of due to the formation of its interface with surface tension $\sigma$ and the energy decrease due to the difference in chemical potential $\Delta\mu$ between the stable and metastable phases; the natural length scale $\sigma\upsilon_m/\Delta\mu$ (where $\upsilon_m$ is the molar volume) dictates the critical nucleus size that distinguishes growing from decaying clusters.

Although the classical nucleation picture may be oversimplified, the qualitative features of its free energy landscape are instructive, particularly when applied to platelet-like volumes of crystal formed from solution. Regarding chain-folded crystals of polymers, this simple picture is extended to allow the fold surface to have a different, and much greater, tension $\sigma_e = \alpha_e\sigma$ ($\alpha_e \approx 10$) than the lateral surfaces [1]. Considering a disk shaped polymer crystal of radius *r* and thickness *l*, the free energy of formation of a lamella from an amorphous melt or solution is then modeled as

$$\Delta G(r, l) = -\pi r^2 l(\Delta\mu / \upsilon_m) + 2\pi r l\sigma + 2\pi r^2\sigma_e . \tag{4.2}$$

In nondimensional form this becomes

$$\Delta G\left(\hat{r}, \hat{l}\right)\frac{\Delta\mu^2}{\pi\upsilon_m^2\sigma^3} = -\hat{r}^2\hat{l} + 2\hat{r}\hat{l} + 2\alpha_e\hat{r}^2 , \tag{4.3}$$

where $\hat{r} = r\,\sigma\upsilon_m/\Delta\mu$ and $\hat{l} = l\,\sigma\upsilon_m/\Delta\mu$. Here we consider $\Delta\mu > 0$, i.e., the sample is below the equilibrium melting temperature or the equilibrium deliquescence solvent activity. As we discuss the relationship between the free energy surface and the growth or dissolution of lamellae, we note again that lamellae are kinetically prevented from evolving strictly along contours of steepest descent, because the thickening process of a lamella is very slow compared to the rate that segments can add or detach from the lateral faces of the lamella. It is, therefore, reasonable to assume that, in response to a step change in $\Delta\mu$, an unstable lamella of size ($r_o$, $l_o$) will rapidly decrease in radius, i.e., the crystallite will either vanish or quickly reach an equilibrium radius, if one exists for $l = l_o$.

Very wide lamella that are thin enough that they are unstable following the step change in $\Delta\mu$ ($\hat{l} < 2\alpha_e$), find their free energy decreases monotonically as they decay in radius (Figure 4.8). On the other hand, very wide lamellae that are thicker ($\hat{l} > 2\alpha_e$) do not decay, since trajectories of decreasing radius would cause their free energy to increase. Since we are interested in the metastability of finite sized clusters, we look for local minima with respect to variations in $\hat{r}$ and $\hat{l}$. Reminiscent of the condensing liquid droplet, there exists a critical size $\hat{r}^* = 2$, $\hat{l}^* = 4\alpha_e$, for which a lamella will neither grow nor decay in width or thickness:

$$\left.\frac{\partial \Delta G}{\partial \hat{l}}\right|_{\hat{r}} \frac{\Delta\mu^2}{\pi\upsilon_m^2\sigma^3} = -\hat{r}^2 + 2\hat{r} = 0 \text{ for } \hat{r}^* = 2, \tag{4.4}$$

$$\left.\frac{\partial \Delta G}{\partial \hat{r}}\right|_{\hat{l}} \frac{\Delta\mu^2}{\pi\upsilon_m^2\sigma^3} = -2\hat{r}\hat{l} + 2\hat{l} + 4\alpha_e\hat{r} = 0 \text{ for } \hat{l}^* = \frac{2\alpha_e\hat{r}}{\hat{r}-1}. \tag{4.5}$$

This is a saddle point in the free energy surface (asterisk in Figure 4.8). No local minima are encountered as a lamella grows or decays radially at constant $\hat{l}$; according to Equation 4.5, $\partial \Delta G / \partial r > 0$ for all $\hat{l} < 2\alpha_e \hat{r} / (\hat{r} - 1)$. Thus, this model cannot explain persistent small lamellar remnants; all lamella that would decay in radius, will decay monotonically until they vanish.

Janeschitz-Kriegl convincingly argues that dangling ends and folds experience greater conformational freedom along the edge of the fold surface than in the crowded interior. He suggests that the effective surface tension $\sigma_e$, therefore, increases sigmoidally as the fold surface area increases [18]. A simple way to capture the essence of this "J-K model" is to divide the fold surface into a core region with high surface tension $\sigma_e = \alpha_e \sigma$ ($\alpha_e \approx 10$) and an annulus of width $\delta_o$ along its perimeter with lower surface tension $\sigma_\delta = \alpha_\delta \sigma$ ($\alpha_\delta \approx 1$) [16] (Figure 4.9).

The free energy of formation of such a lamellar disk can be expressed in non-dimensional form as

$$\Delta G_{J-K}\left(\hat{r}, \hat{l}\right) \frac{\Delta\mu^2}{\pi \upsilon_m^2 \sigma^3} = \begin{cases} -\hat{r}^2 \hat{l} + 2\hat{r}\hat{l} + 2\alpha_e \left(\hat{r} - \hat{\delta}_o\right)^2 + 2\alpha_\delta \left(\hat{r}^2 - \left(\hat{r} - \hat{\delta}_o\right)^2\right) & ; \ \hat{r} > \hat{\delta}_o \\ -\hat{r}^2 \hat{l} + 2\hat{r}\hat{l} + 2\alpha_\delta \hat{r}^2 & ; \ \hat{r} \le \hat{\delta}_o \end{cases} . \quad (4.6)$$

The resulting contours of metastability with respect to changes in $\hat{r}$ and $\hat{l}$ are defined by

$$\left.\frac{\partial \Delta G_{J-K}}{\partial \hat{l}}\right|_{\hat{r}} \frac{\Delta\mu^2}{\pi \upsilon_m^2 \sigma^3} = 0 \text{ for } \hat{r}^* = 2 \quad (4.7)$$

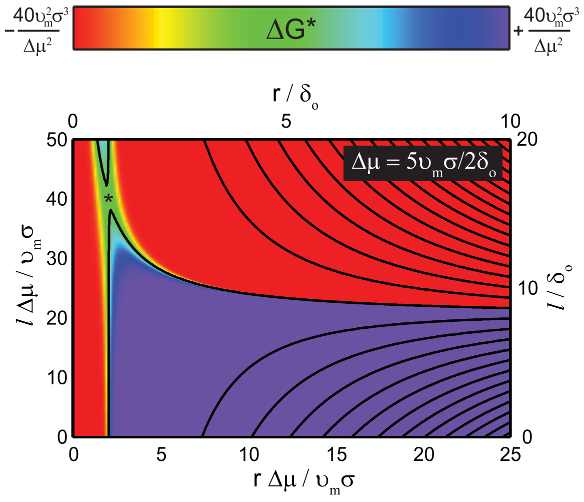

Figure 4.8. Contour map of ΔG (Equation 4.3) with $\alpha_\delta = 1$, $\alpha_e = 10$, and $\Delta\mu = 5\upsilon_m\sigma/2\delta_o$. Bottom and left axes are normalized by the characteristic lengthscale $\sigma\upsilon_m/\Delta\mu$. Top and right axes are normalized by a constant length $\delta_o$. The color scale saturates at $\pm$ 40 $\upsilon_m^2\sigma^3/\Delta\mu^2$ relative to the saddle point free energy $\Delta G^*$ for emphasis. Equipotential contours are equally spaced.

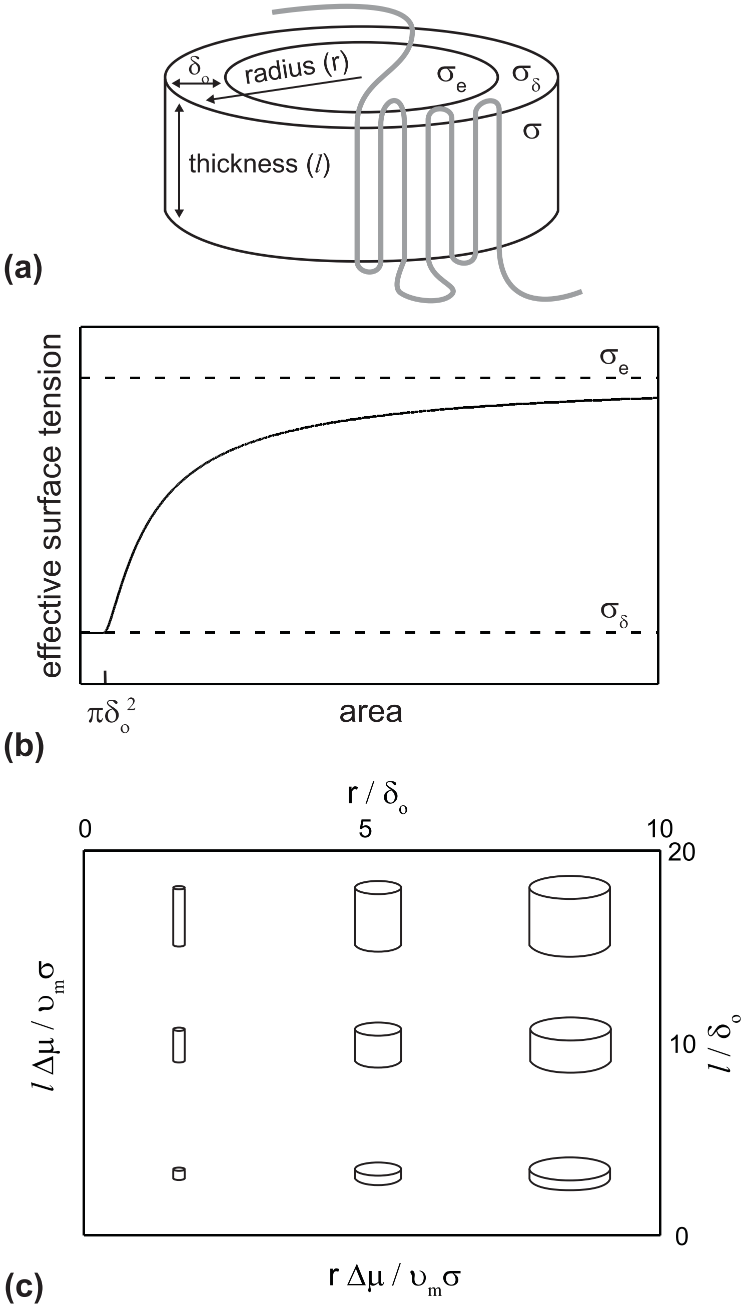

Figure 4.9. (a) Schematic of a disk shaped lamellar crystal of thickness *l* and radius *r* and three distinct surface tensions ($\sigma$, $\sigma_e$, and $\sigma_\delta$). An annulus of width $\delta_o$ defines the low energy perimeter of the fold surface. (b) Average surface tension of the fold surface as a function of the fold surface area. (c) Schematic indicating the aspect ratio of lamellar crystals in various regions of the contour maps of Figures 4.8 and 4.10. The diagonal represents crystals with $l = 2r$.

and

$$\left.\frac{\partial \Delta G_{J-K}}{\partial \hat{r}}\right|_{\hat{l}} \frac{\Delta\mu^2}{\pi \upsilon_m^2 \sigma^3} = 0 \text{ for } \hat{l}^* = \begin{cases} \dfrac{2\alpha_e \hat{r} - 2\hat{\delta}_o\left(\alpha_e - \alpha_\delta\right)}{\hat{r}-1} & ; \hat{r} > \hat{\delta}_o \\ \dfrac{2\alpha_\delta \hat{r}}{\hat{r}-1} & ; \hat{r} \le \hat{\delta}_o \end{cases} . \tag{4.8}$$

In the limit of infinite $\hat{r}$, lamellae still decay in radius when $\hat{l} < 2\alpha_e$. However, under certain conditions, the free energy reaches a local minimum as the radius decreases at fixed lamellar thickness. This occurs when the product of the change in interfacial energy across the fold surface and the annulus thickness is sufficiently large:

$$(\alpha_e - \alpha_\delta)\hat{\delta}_o = (\alpha_e - \alpha_\delta)\frac{\delta_o \Delta\mu}{\upsilon_m \sigma} > \alpha_e . \tag{4.9}$$

In this case, a wide, thin lamella will rapidly decrease in radius until it reaches the valley in the free-energy landscape near $\hat{r} = \hat{\delta}_o$ and then slowly changes in thickness. Note that the contour defined by $\hat{l} = 2\alpha_e \hat{r} /(\hat{r} - 1)$ in the traditional model defines a ridge, whereas the contour defined by $\hat{l} = 2\alpha_e \hat{r} - 2\hat{\delta}_o(\alpha_e - \alpha_\delta)/(\hat{r} - 1)$ in the J-K model defines a valley (c.f. Figure 4.8 and Figure 4.10). Local minima with respect to changes in radius, therefore, exist only in the free energy landscape defined by the J-K model.

As the depth of metastability, Δμ, decreases (corresponding to increasing $a_w$ or temperature), we observe two expected trends in the J-K free energy landscape: (i) the stability of crystals of a given thickness decreases, i.e., thicker crystals dissolve or melt, and (ii) the saddle point,

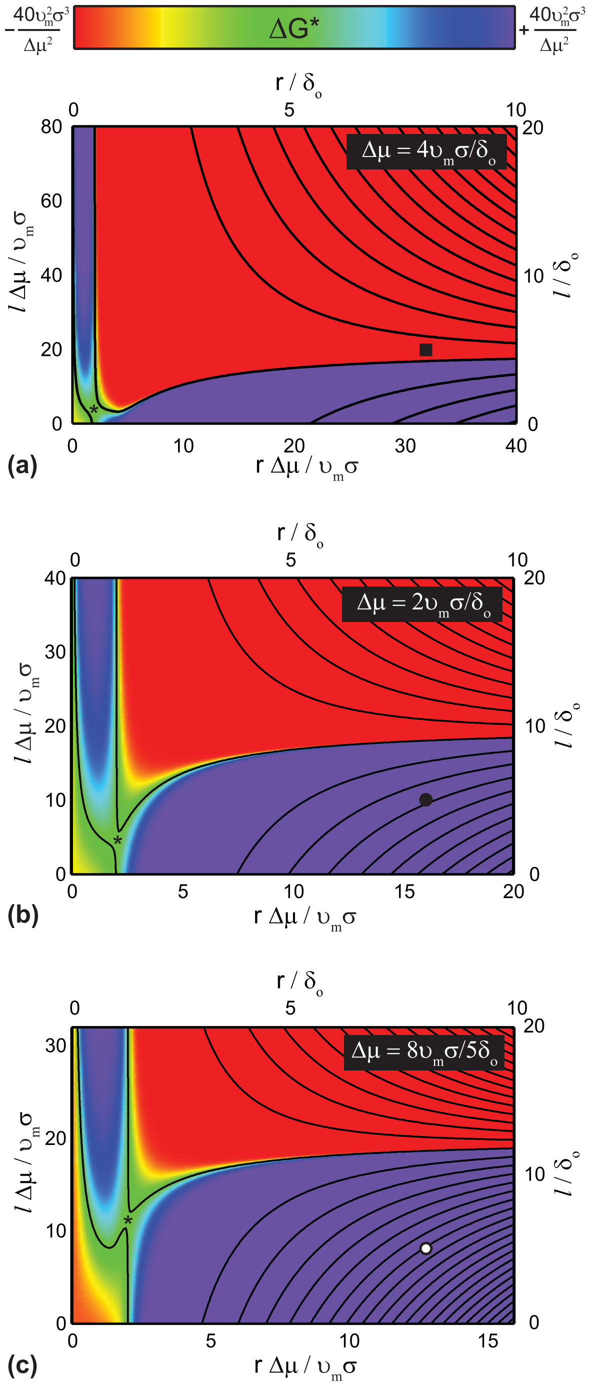

Figure 4.10. Contour maps of $\Delta G_{J\text{-}K}$ (Equation 4.6) with $\alpha_\delta = 1$, $\alpha_e = 10$, and (a) $\Delta\mu = 4\upsilon_m\sigma/\delta_o$, (b) $\Delta\mu = 2\upsilon_m\sigma/\delta_o$, (c) $\Delta\mu = 8\upsilon_m\sigma/5\delta_o$. Bottom and left axes are normalized by the characteristic lengthscale $\sigma\upsilon_m/\Delta\mu$. Top and right axes are normalized by a constant length $\delta_o$. The symbols ■, ●, and ○ indicate identical lamellae with $r = 8/\delta_o$ and $l = 5/\delta_o$.

$$\hat{r}^* = 2 \text{ and } \hat{l}^* = 4\alpha_e - 2\frac{\delta_o \Delta\mu}{\upsilon_m \sigma}\left(\alpha_e - \alpha_\delta\right), \tag{4.10}$$

shifts to greater thickness, i.e., the lowest energy path to formation of a stable crystalline entity from the melt or solution requires greater crystal thickness. We also notice changes in the detailed shape of the saddle with decreasing $\Delta\mu$, which affects how trapped clusters evolve in thickness. When $\Delta\mu = 4\upsilon_m\sigma/\delta_o$ or $\Delta\mu = 2\upsilon_m\sigma/\delta_o$ (Figures 4.10a and 4.10b), a local minimum with respect to changes in radius only occurs for lamellar thicknesses that are greater than the saddlepoint value ($\hat{l} > \hat{l}^*$), i.e., the lamellar remnants that can be trapped in the free energy landscape of Figures 4.10a and 4.10b already start with sufficient thickness that they will thicken further. On the other hand, when $\Delta\mu = 8\upsilon_m\sigma/5\delta_o$ (Figure 4.10c), a local minimum with respect to changes in radius also exists for some values of $\hat{l} < \hat{l}^*$. Thus, in the landscape of Figure 4.10c, the thickness of trapped clusters may increase or decrease, depending on the initial thickness of the lamella that is dissolving.

To illustrate the dynamics of lamellae under various conditions, consider a lamella with thickness $l = 5\delta_o$ and radius $r = 8\delta_o$ on each of the three free energy surfaces of Figure 4.10 (indicated by ■, ●, and ○). As discussed previously, the kinetics of changing radius are much faster than the kinetics of changing thickness, and so the initial trajectory of the lamella can be reasonably estimated by examining a sectional view of the surface at fixed $l = 5\delta_o$ (Figure 4.11a). For the deepest supersaturation, $\Delta\mu = 4\upsilon_m\sigma/\delta_o$ (A in Figure 4.11a), the lamella grows radially; but a lamella of this thickness dissolves at the two shallower supersaturations, $\Delta\mu = 2\upsilon_m\sigma/\delta_o$ and $\Delta\mu = 8\upsilon_m\sigma/5\delta_o$ (B and C in Figure 4.11a), and its radius decreases until it reaches a local free energy minimum. The coordinate of the trapped cluster in each case has been indicated on an expanded view of the free energy saddle for conditions B and C (Figure 4.11b and 4.11c). Cluster B has a thickness $\hat{l} > \hat{l}^*$ and reduces its free energy by slowly evolving toward increased thickness and radius. Cluster C has a thickness $\hat{l} < \hat{l}^*$ and reduces its free energy by slowly evolving toward decreased thickness and radius.

## 4.5 CONCLUSIONS

Memory effects analogous to those documented in polymer melts have been observed in aqueous solutions of polyethylene oxide by SAGA. Remnants of lamellar crystals—likely clusters containing a small number of segments and folds—persist for long times beyond the apparent dissolution point and slowly evolve toward increasing or decreasing axial thickness under certain conditions. A new thermodynamic model that accounts for reduced interfacial energy along the perimeter of the lamellar fold surface captures both the metastability and dynamics of these remnants.

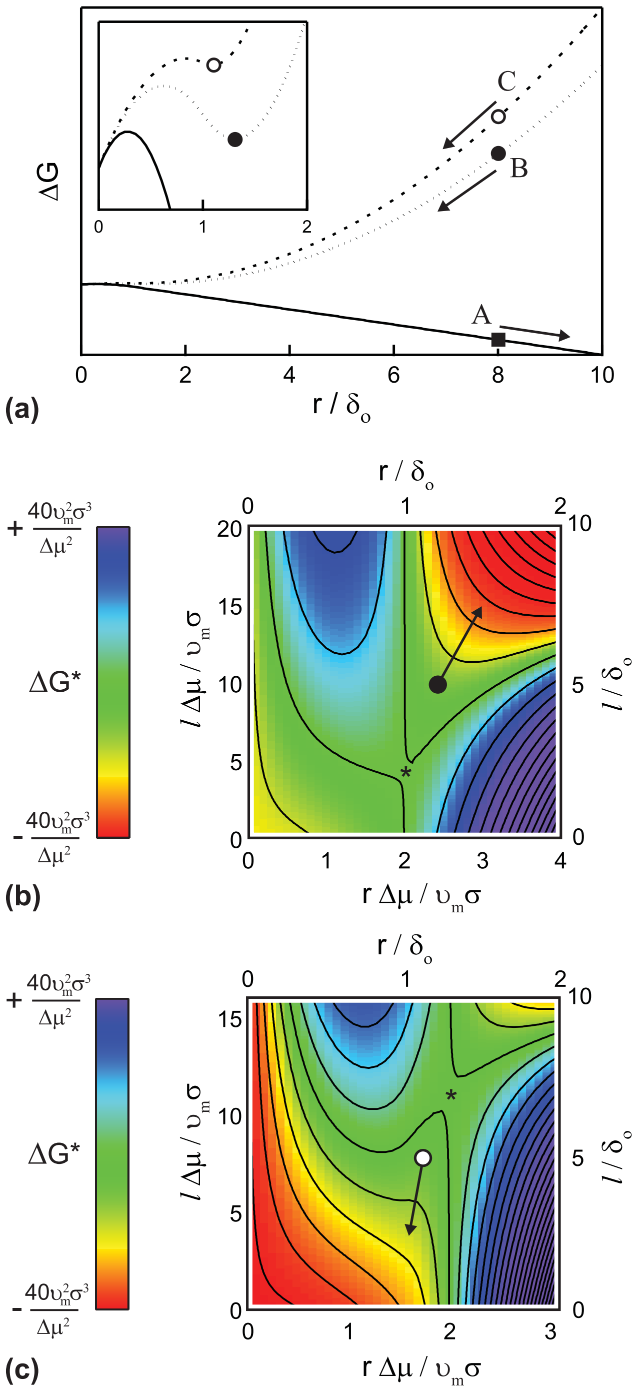

Figure 4.11. (a) $\Delta G_{J\text{-}K}$ as a function of radius for constant $l = 5\delta_o$ for the conditions of Figures 4.10a (A, ■), 4.10b (B, ●), and 4.10c (C, ○). The inset depicts an expanded view at small radius, revealing local minima that trap clusters B and C at finite radius. Also, expanded views of the saddles in (b) Figure 4.10b and (c) 4.10c that trap a cluster under conditions in which they reduces their free energy by (b) increasing and (c) decreasing in thickness.

# REFERENCES

1 J. D. Hoffman, G. T. Davis, J. I. Lauitzen Jr., *The rate of crystallization of linear polymers with chain folding.* In *Treatise on solid state chemistry*; N. B. Hannay, Ed.; Plenum: New York, 1976; vol. 3, ch. 7.

2 R. Verma, H. Marand, B. Hsiao, *Macromolecules* 29, 7767 (1996).

3 H. Marand, Z. Huang, *Macromolecules* 37, 6492 (2004).

4 M. I. Abo el Maaty, D. C. Bassett, *Polymer* 46, 8682 (2005).

5 D. J. Blundell, A. Keller, A. J. Kovacs, *Polymer Let* 4, 487 (1996).

6 B. Fillon, J. C. Wittman, B. Lotz, A. Thierry, *J. Polymer Sci.* 31, 1383 (1993).

7 Y. Feng, X. Jin, *J. Appl. Poyml. Sci.* 72, 1559 (1999).

8 M. V. Massa, M. S. M. Lee, K. Dalnoki-Veress, *J. Polym. Sci B Polym. Phys.* 43, 3438 (2005).

9 G. C. Alfonso, A. Ziabicki, *Col. Polym. Sci.* 273, 317 (1995).

10 G. C. Alfonso, P. Scardigli, *Macromol. Symp.* 118, 323 (1997).

11 R. J. Lehnert, H. Hirschmann, *Polymer Journal* 29, 100 (1997).

12 T. Sasaki, Y. Yamamoto, T. Takahashi, *Polymer Journal* 32, 263 (2000).

13 A. Häfele, B. Heck, T. Hippler, T. Kawai, P. Kohn, G. Strobl, *Eur. Phys. J. E* 16, 217 (2005).

14 J. C. Fischer, J. H. Hollman, D. Turnbull, *J. Appl. Phys.* 19, 775 (1948).

15 A. Ziabicki, G. C. Alfonso, *Col. Polym. Sci.* 272, 1027 (1994).

16 H. Janeschitz-Kriegl, *Col. Polym. Sci.* 275, 1121 (1997).

17 H. Janeschitz-Kriegl, E. Ratajski, H. Wippel, *Col. Polym. Sci.* 277, 217 (1999).

18 H. Janeschitz-Kriegl, *Col. Polym. Sci.* 281, 1157 (2003).

19 Chapter 3 of this thesis.

20 Chapter 2 of this thesis.

21 H. C. van de Hulst, *Light Scattering by Small Particles*; Wiley: New York, 1957.

22 H. Marand, J. Xu, S. Srinivas, *Macromolecules* 31, 8219 (1998).

23 R. Becker, W. Döring, *Ann. Phys.* 24, 719 (1935).

24 J. H. Seinfeld, S. N. Pandis, *Atmospheric Chemistry and Physics*; Wiley: New York, 1998.

*Chapter 5*

# FUTURE DIRECTIONS

## 5.1 PARTICLE RE-CAPTURE AND IMAGING

A levitated polymer sample may be re-captured after crystallization for *ex-situ* analysis (optical microscopy, TEM, SEM) by directing it toward the removable portion of the bottom electrode with a properly adjusted electric field (Chapter 2). Imaging will enable characterization of the semicrystalline morphology (nucleation density, lamellar thickness, degree of crystallinity) as a function of crystallization conditions to complement the gravimetric data.

## 5.2 IMPROVING THE RESPONSE TIME OF THE HUMIDIFICATION SYSTEM

The humidification system described in Chapter 2 has a finite response time, which imposes an upper bound on the rate at which the solute concentration of an aqueous solution can be changed (see Appendix B for calibration experiments). Although we have reported exciting observations in Chapter 3 and Chapter 4 utilizing slow constant rate scans, it may be desirable to design future experiments in which the activity of water is also rapidly adjusted to unambiguously characterize a given thermodynamic state. The lag in response to imposed changes in humidity likely result from equilibration with hygroscopic surfaces inside either the levitation chamber or the proportional solenoid valve that modulates the chamber pressure. If these materials issues cannot be resolved, one may employ a humidification technique that utilizes an atmosphere of pure water [1, 2]. This modification requires high vacuum capabilities, but will be insensitive to surface sorption that limits the present technique.

## 5.3 POLYMER CRYSTAL NUCLEATION FROM THE MELT

Crystallization of PEO reported in Chapter 3 and Chapter 4 occurred in supersaturated aqueous solution droplets at room temperature. The electrostatic particle levitator described in Chapter 2, however, is also equipped to investigate crystal nucleation kinetics from the melt. The temperature of the levitation chamber, and thus the particle, is strictly regulated by recirculating heat transfer fluid (between –25 and 125 °C), enabling thermal cycling of particles between the semicrystalline and molten states. Since the mass of a polymer particle does not vary during thermal cycling, phase transitions must be detected by changes in optical properties. In a preliminary experiment, a PEO particle was heated to 75 °C (m.p. = 63 – 65 °C) for several hours and then cooled to 23 °C. Images of angular light scattering (Chapter 2) were recorded for more than 14 hours following the temperature quench (Figure 5.1). After approximately 10 hours, an abrupt change in the scattering pattern indicated that the molten droplet (at a subcooling of 40 °C) suddenly crystallized as a result of a nucleation event. (Crystallization temperatures below 5 °C are routinely required to induce immediate nucleation of dry PEO.) Prior to crystallization the majority of the light scattering images exhibited uniform vertical bands characteristic of Mie scattering, although, occasionally, images were slightly distorted by diagonal disturbances. After crystallization, however, the Mie pattern in all recorded images was severely distorted because of optical anisotropy, and perhaps surface roughness, introduced by crystallization.

These results confirm that light scattering can be used to detect crystallization from the melt, enabling statistical measurements of nucleation kinetics analogous to the aqueous sodium chloride experiments presented in Chapter 2. Of even greater interest, however, are the minor distortions exhibited in many images of the metastable molten droplet prior to crystallization since they may be caused by the stochastic appearance of subcritical embryos of the stable crystalline phase. Further investigation will benefit from a deeper understanding of how light scattering is influenced by inclusions and surface distortions [3-10]. It has also been suggested that modifying the experimental setup to measure the elements of the Stokes vector (a four element vector that unambiguously characterizes the polarization of light) in the exact backscattered direction would enable greater sensitivity to deviations from the ideal spherical scatterer [11].

Mie images of molten PEO droplet prior to crystallization

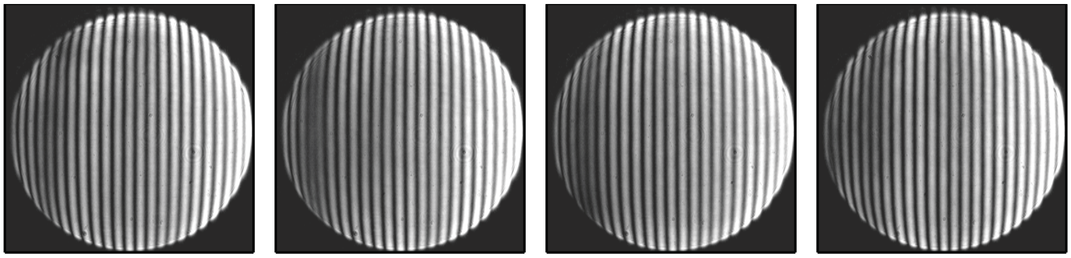

Slightly distorted Mie images of molten PEO droplet prior to crystallization

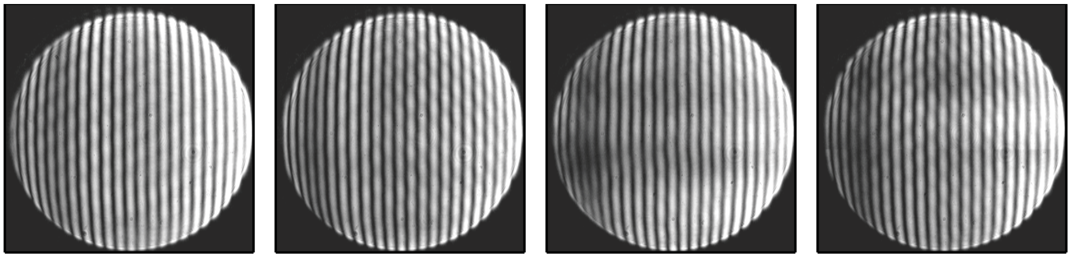

Severely distorted Mie images of PEO particle after crystallization

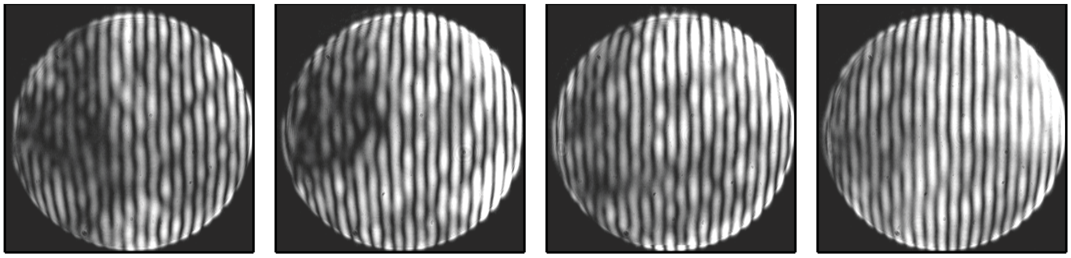

Figure 5.1. Representative light scattering images of a PEO particle before and after crystallization from a room temperature melt.

# REFERENCES

1 C. B. Richardson, J. F. Spann, *J. Aer. Sci.* 15, 563 (1984).

2 I. N. Tang, H. R. Munkelwitz, *J. Coll. Int. Sci.* 98, 430 (1984).

3 A. Ashkin, J. M. Dziedzic, *App. Opt.* 19, 660 (1980).

4 A. Mugnai, W. J. Wiscombe, *App. Opt.* 25, 1235 (1985).

5 A. Mugnai, W. J. Wiscombe, *App. Opt.* 27, 2405 (1988).

6 A. Mugnai, W. J. Wiscombe, *App. Opt.* 28, 3061 (1989).

7 K. Muinonen, *J. Quant. Spectrosc. Radiat. Transfer* 55, 603 (1996).

8 D. R. Secker, P. H. Kaye, R. S. Greenaway, E. Hirst, D. L. Bartley, G. Videen, *App. Opt.* 39, 5023 (2000).

9 G. Videen, W. Sun, Q. Fu, D. R. Secker, R. S. Greenaway, P. H. Kaye, E. Hirst, D. Bartley, *App. Opt.* 39, 5031 (2000).

10 D. R. Prabhu, M. Davies, G. Videeen, *Opt. Express* 8, 308 (2001).

11 Matthew Berg and Chris Sorensen, Kansas State University, private communication (2005).

# *Appendix A*

# INSTRUMENTATION NOTES

## A.1 SOFTWARE

The instrument described in Chapter 2 is operated by software programmed in LabView (v.5.1). The essential features include acquisition of particle image in three dimensions for calculating position, PID control of particle position, PID control of relative humidity, acquisition of the angular scattering pattern, and data acquisition (vertical balancing voltage, relative humidity, and chamber temperature are saved to .txt files at a prescribed frequency). The setpoint for the RH controller can be programmed for arbitrary history, enabling automated experiments that require minimal attention. The sodium chloride nucleation experiment described in Chapter 2, for example, was performed over 5 days while the graduate student was out of town.

## A.2 ELECTRONICS

The instrument described in Chapter 2 is integrated with a PC with data acquisition hardware. The NI 6013 device (National Instruments) handles analog inputs. The NI 6703 device (National Instruments) handles analog outputs. The NI 1407 device (National Instruments) handles capture of angular light scattering images from a CCD video camera. The Raven device (Bitflow) handles capture of particle images from up to four linescan cameras. The NI 6703 and NI 1407 are also capable of digital input/output.

Several analog circuits have been fabricated for voltage and power amplification to facilitate instrument control by a PC. A DC amplification circuit allows application of balancing potentials up to ± 300 V across the top and bottom electrodes with ± 10 V (Figures A.1 and A.2). An AC power supply creates a high voltage (up to 2 kV rms), variable frequency (20 – 300 Hz) AC potential that is applied to the rod electrodes for electrodynamic particle focusing and a DC bias is applied to the AC potential to enable electrostatic compensation by opposing pairs of rods (Figure A.3). Mechanical relays are used to activate/deactivate the AC field and to control the flow of recirculating heat fluid (Figure A.4). Proportional solenoid valves are driven by transistor amplifiers (Figure A.5). A timer circuit sets the framerate and exposure time of the imaging linescan cameras (Figure A.6).

## A.3 PARTICLE IMAGING AND POSITION CONTROL

The particle imaging and position control system described in Chapter 2 is extremely sensitive and robust. However, as with any engineering project, we have learned much since our initial design, and we can now recommend changes that would enable even greater performance at reduced cost. Linescan cameras were selected for particle imaging because they enable extremely fast framerates (approximately 10 kHz compared with the 30 Hz framerate of a typical CCD video camera); we anticipated the need for control at greater than 30 Hz. Successful integration of these cameras with a framegrabber proved to be quite difficult and time consuming. We also later realized that 30 Hz is sufficient for 3D electrostatic feedback control of particles with diameter less than 100 microns (we have no experience with larger particles), although the linescan cameras are typically operated at 40 Hz. Therefore, if the linescan cameras of the current instrument need replacement, or if another instrument is

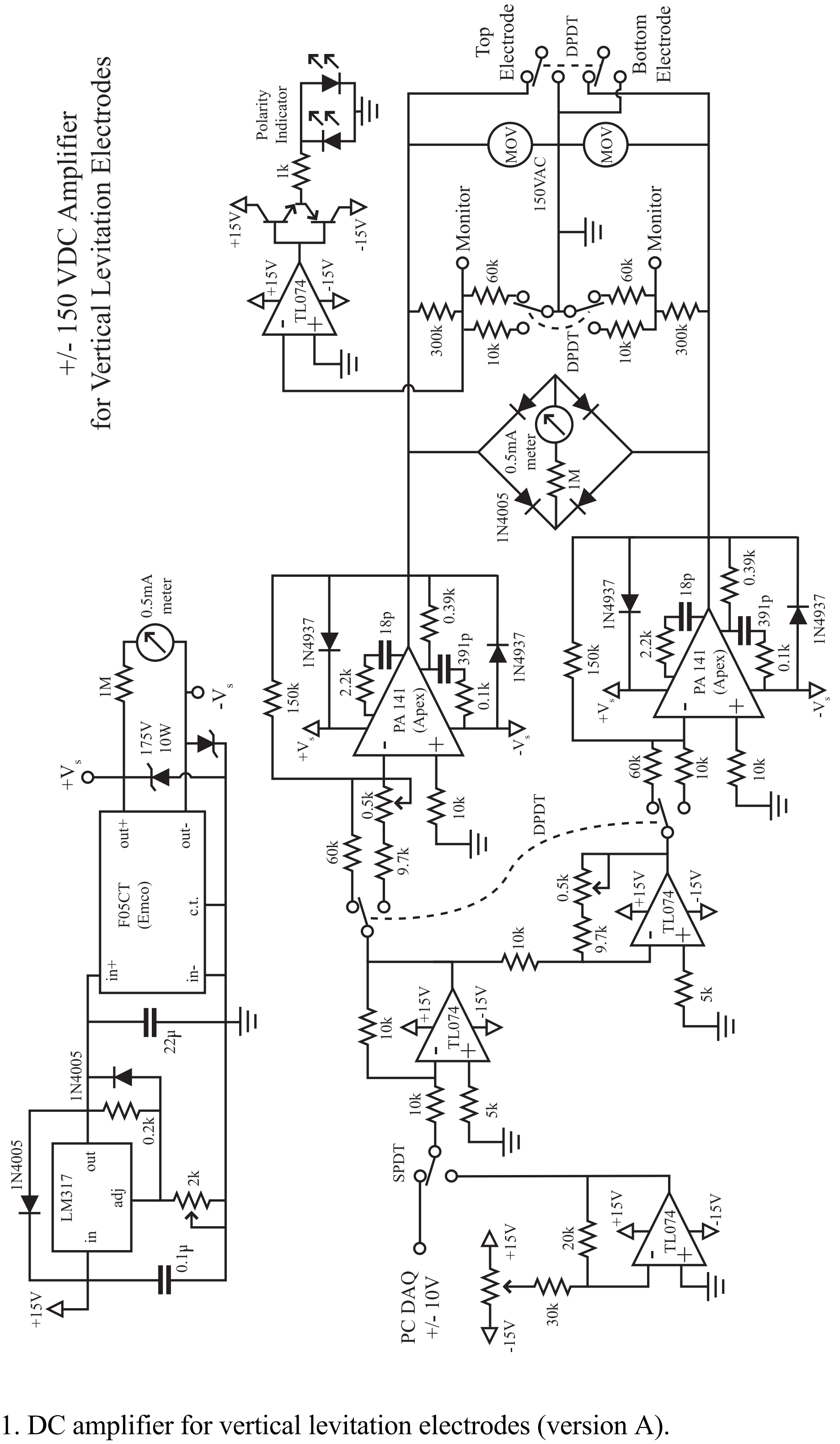

Figure A.1. DC amplifier for vertical levitation electrodes (version A).

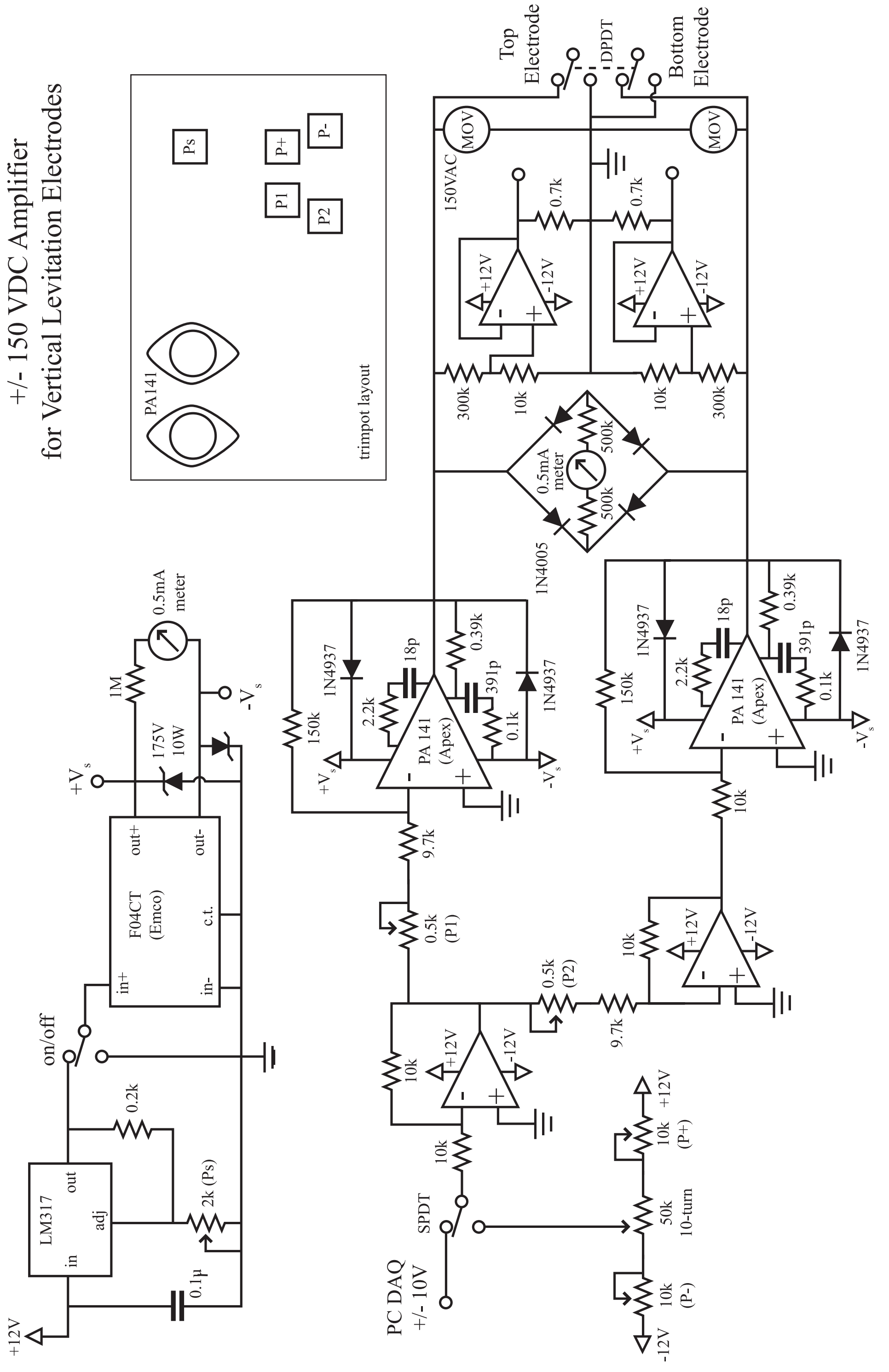

Figure A.2. DC amplifier for vertical levitation electrodes (version B).

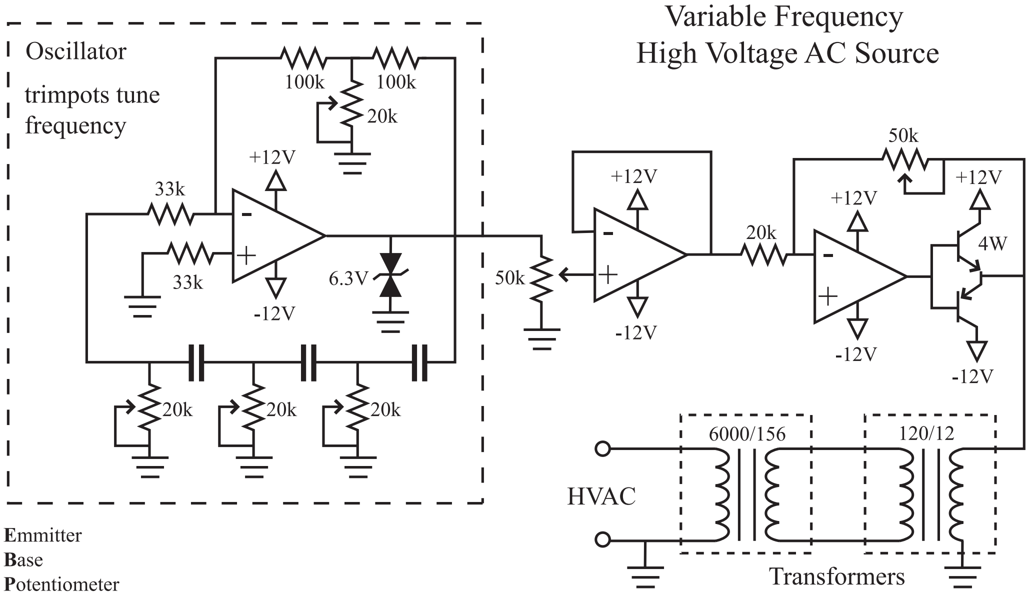
Variable Frequency High Voltage AC Source

**E**mmitter
**B**ase
**P**otentiometer
**F**eedback Pot
Pot. **W**iper
**G**round
**RC** Pots
**C**apacitors

30 pin connector assignments on circuit board
(pairs are shorted except for Cap's)

| | | | | | | | | | | | | | | |
|---|---|---|---|---|---|---|---|---|---|---|---|---|---|---|
| ☒ | E | B | P | F | W | $V_-$ | G | $V_+$ | R | C | R | C | R | C |

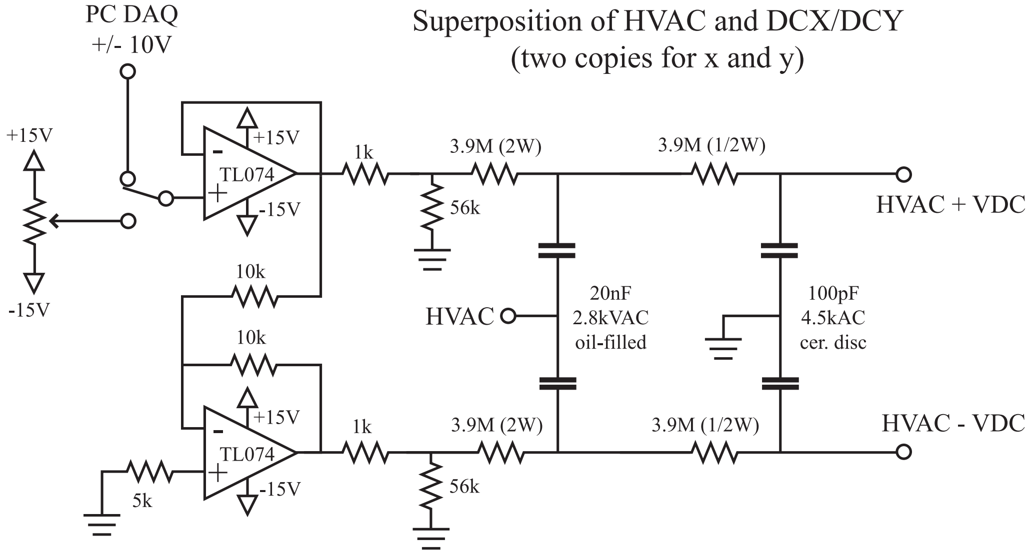
Superposition of HVAC and DCX/DCY
(two copies for x and y)

Figure A.3. Variable frequency high voltage AC source and DC superposition.

High Voltage Relay for PC control of AC potential

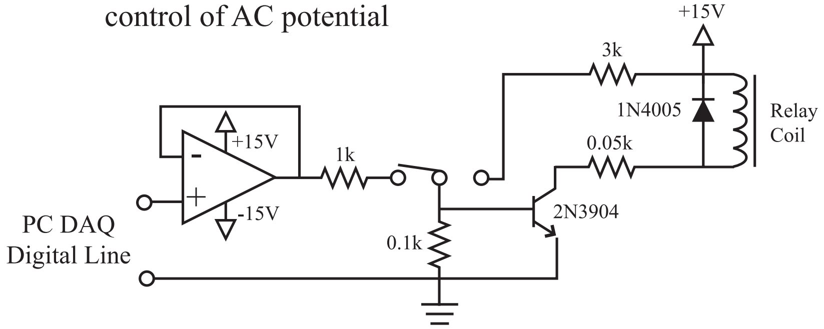

Relay for PC control of recirculating heat fluid

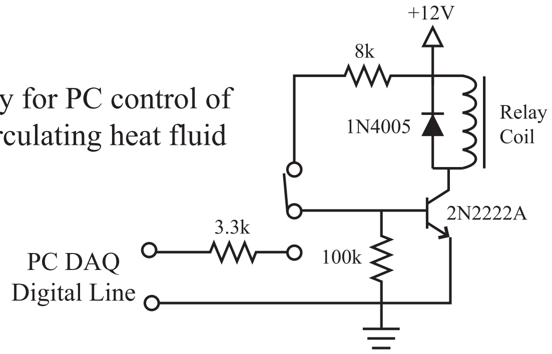

Figure A.4. Transistor amplifiers to drive mechanical relays.

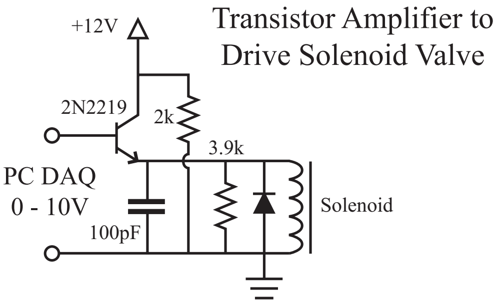

Figure A.5. Transistor amplifiers to drive proportional solenoid valves.

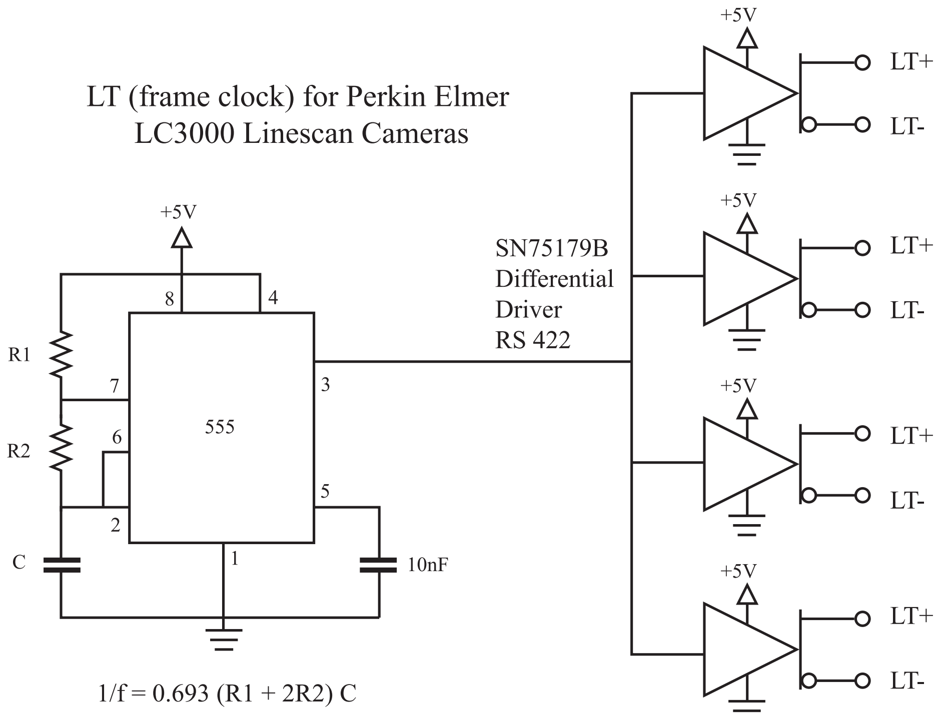

Figure A.6. Timing circuit for linescan camera framerate and exposure.

fabricated, we recommend using two or three CCD video cameras instead. This modification would eliminate the need for a cylindrical element in the optical path and would thus enhance the image intensity, allowing observations of smaller particles. A framegrabber would be required to calculate a 2D position from a single camera (the Bitflow Raven currently acquiring from the linescan cameras would suffice). Three CCD cameras can be implemented without a framegrabber if the output of each is appropriately filtered (Figure A.7) and digitized at greater than 6 kHz by data acquisition hardware. The analog filtering circuit senses the peak pixel intensity in each row, essentially transforming the 2D array to a vertical 1D array. Unlike linescan detectors, which have a width of 1 pixel (ca. 14 microns), this "1D detector" is hundreds of pixels wide and so does not require that the particle be imaged as a line.

## A.5 THERMAL REGULATION

The environmental control module described in Chapter 2 enables robust control of relative humidity inside the levitation chamber. Although temperature is also strictly regulated, it can only be set below ambient. A recirculating heat transfer fluid keeps the Nafion humidifier, the Vaisala humidity sensor, and the chamber at the same temperature, but the temperature of all other plumbing is unregulated. This forbids operation at high humidity above ambient temperature since water would condense in the cool lines. Experiments at elevated temperature would require modifications that enable thermal control of the entire module.

## A.6 PARTICLE CAPTURE

One microparticle must be isolated in the electrodynamic field before three-dimensional electrostatic feedback control is activated. The following procedure enables capture of only

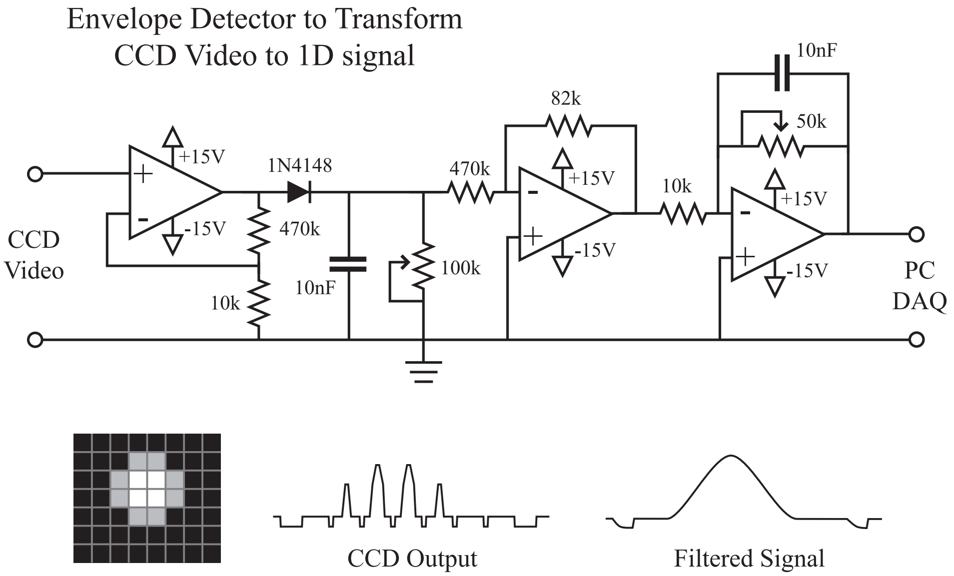

Figure A.7. Envelope detector to transform CCD video to 1D signal.

solid particles. Although others have reported reproducible capture of charged liquid microdroplets, we have not attempted to because of the high viscosity of polymer solutions or melts. A small amount of powder is placed on the tip of an 1/8" Plexiglas rod that has a step machined at the end to fit through the hole in the bottom DC electrode. The rod is then inserted into the chamber so that the tip extends just beyond the electrode surface. With the AC electric field adjusted safely below breakdown levels, a mechanical shock to the rod launches one or more particles into stable oscillation. After careful removal of the injection rod, proper adjustment of the DC electric field eliminates vertical oscillations of a target particle. A particle is typically selected based on desired charge-to-mass ratio or size; the dry balancing voltage must be sufficiently small so that the maximum balancing voltage of the DC power supply is not exceeded after deliquescence. Temporary reduction of the AC electric field strength then allows any unbalanced particles to float out of the viewing volume. When only one particle remains, three-dimensional electrostatic feedback control is activated and the AC electric field completely eliminated; a high voltage relay enables software activation/deactivation of the AC field. During an experiment the access hole is plugged by a delrin rod with a stainless steel cap that is sealed to the chamber with an o-ring.

# *Appendix B*

## CALIBRATION FOR CONSTANT SCAN RATE AT HIGH RH

The relative humidity, or activity of water ($a_w$), inside the particle levitation chamber is controlled by modulating the pressure of a nitrogen stream that contains a fixed mole fraction of water vapor such that:

$$a_w = a_{w,o}(\mathrm{p}/\mathrm{p_o}) \tag{B.1}$$

where $a_{w,o}$ is the activity of water in the nitrogen stream recorded at atmospheric pressure ($\mathrm{p_o}$) by a humidity sensor, and p is the absolute pressure inside the chamber recorded by a pressure transducer. Accuracy of Equation B.1 requires that the mole fraction of water vapor inside the chamber is identical to that at the humidity sensor. As humidity increases, however, there is an increasing likelihood that water is sorbed by surfaces within the apparatus, introducing capacitance that prevents very rapid changes in $a_w$. The actual instrument response to imposed changes in $a_w$ was measured during continuous (Figure B.1) and stepwise (Figure B.2) scans with an aqueous sodium chloride droplet, which maintains equilibrium with the surrounding atmosphere. Discrepancy in the measured mass between continuous scans up and down in $a_w$ was used to quantify the lag and derive a correction that was applied to the PEO data in the main text. The difference in water activity between that recorded during the up scan ($a_{w,up}$) and down scan ($a_{w,dn}$) at a given $\mathrm{m/m_o}$ for $4 < \mathrm{m/m_o} < 11$ was determined from the data in Figure B.1. Since the equilibration time exhibited in Figure B.2 is symmetric with respect to a steps up and down in activity, we assume that the actual activity is $a_w = (a_{w,up} + a_{w,dn})/2$, and, therefore, the data requires a lag correction of $\Delta a_w = (a_{w,up} - a_{w,dn})/2$; $\Delta a_w$ increases with increasing $a_w$ for $a_w > 0.79$ (Figure B.3). A linear fit to the data in Figure B.3 was used to correct for the hysteresis exhibited in the continuous scan at high activity (Figure B.4). The corrected data displays no hysteresis and agrees well with the four equilibrium data points determined from the stepwise scan.

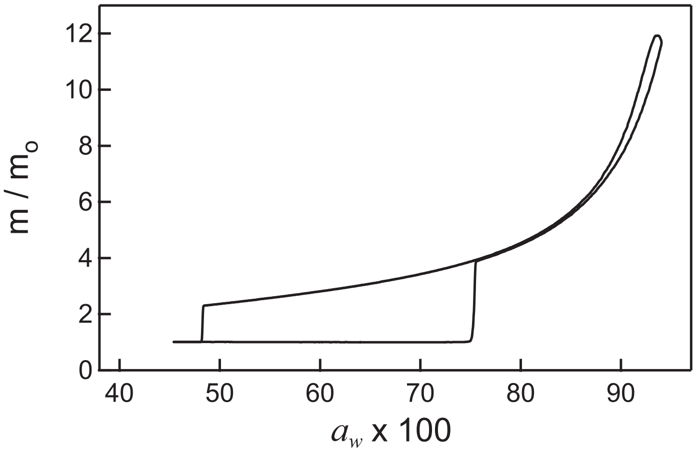

Figure B.1. Response of a sodium chloride particle to a continuous triangular scan in water activity between 0.45 and 0.93 at 0.04 $hr^{-1}$. T = 21.10 ± 0.05 °C.

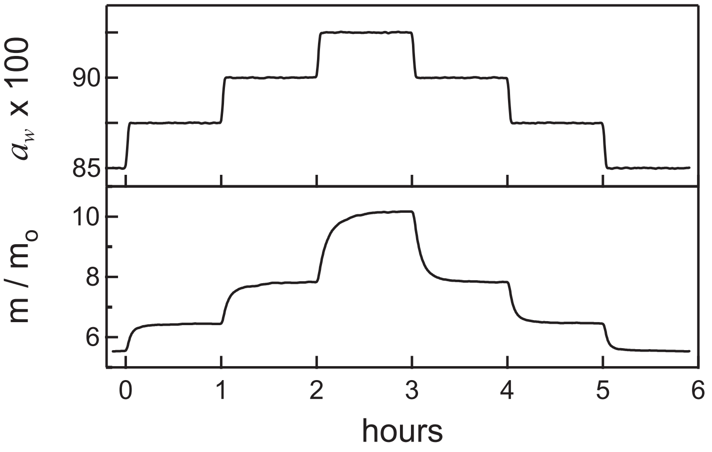

Figure B.2. Response of a sodium chloride particle to a stepwise scan in water activity between 0.850 and 0.925. T = 21.10 ± 0.05 °C.

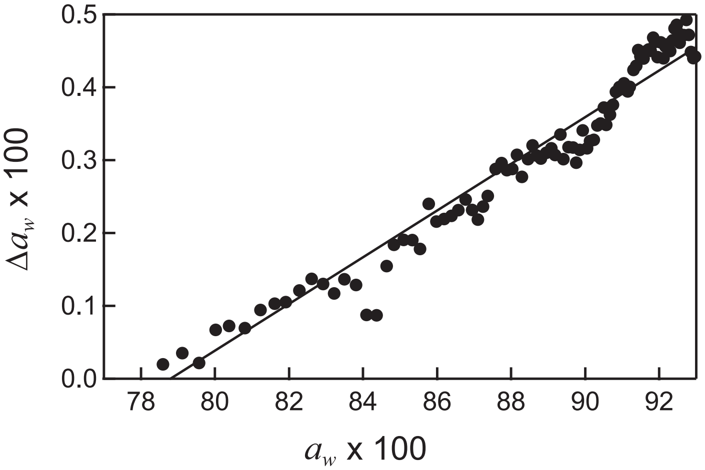

Figure B.3. Estimation of the lag in activity as a function of nominal activity during a linear scan at 0.04 $hr^{-1}$.

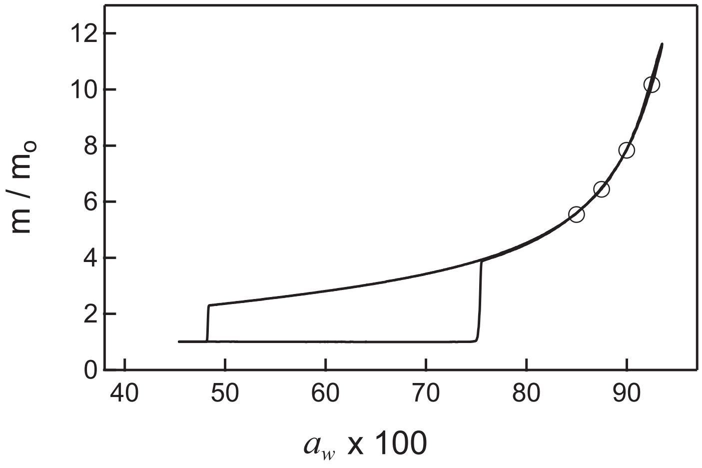

Figure B.4. Data from Figure B.1 corrected for lag. Open circles denote equilibrium data points from Figure B.2.